CZECH TECHNICAL UNIVERSITY IN PRAGUE

Faculty of Nuclear Sciences and Physical Engineering

Department of Physics
Branch: Physical Engineering
Specialization: Physics and Technology of Nuclear Fusion

Advanced Laser-Plasma Based Sources of Accelerated Particles

Bachelor's Degree project

Author: **Jan Prokůpek**
Supervisor: **Dr. Daniele Margarone, PhD.**
Year: **2009**

Prohlášení

Prohlašuji, že jsem svou bakalářskou práci vypracoval samostatně a použil jsem pouze podklady uvedené v přiloženém seznamu.

Nemám závažný důvod proti užití tohoto školního díla ve smyslu §60 Zákona č. 121/2000 Sb., o právu autorském, o právech souvisejících s právem autorským a o změně některých zákonů (autorský zákon).

V Praze, dne 7.7.2009 Jan Prokůpek

Acknowledgements

I would like to express my thanks to Dr. Daniele Margarone for his invaluable support, patience, encouragement, supervision and useful suggestions throughout this work. His moral support and guidance enabled me to complete my work successfully.

Title: **Advanced Laser-Plasma Based Sources of Accelerated Particles**
Author: Jan Prokůpek

Branch: Physical Engineering
Work: Bachelor's Degree project

Supervisor: Dr. Daniele Margarone, PhD.
Department of X-ray Lasers
Institute of Physics of the AS CR

Abstract:

High energy particles can be accelerated by means of high intensity laser beams - target/plasma interaction via non-linear forces. Recent progress in laser technology enables producing highly collimated quasi-monoenergetic electron beams and high current ion beams. A design of an experimental setup along with precise description of its parts is the first step to achieve best results. Charged particle beams can be deflected by static electric and magnetic fields and further detected by sets of devices which have to be calibrated in proper way. One of the measuring techniques for the ion beam energy is a time of flight method which can also give information about the particle beam intensity. Laser-plasma based particle accelerators can find applications in various areas of different scientific, industrial and societal fields.

Key words: laser, plasma, particle accelerators, electron and ion streams, high energy particle diagnostics.

Název práce: **Moderní urychlovače částic na bázi laserového plazmatu**
Autor: Jan Prokůpek

Abstrakt:

Částice mohou být urychleny na vysoké energie pomocí nelineárních sil během interakcí terče/plazmatu s laserovými paprsky o vysoké intenzitě. Nedávný pokrok v laserové technologii umožnil produkci vysoce kolimovaných kvazimonoenergetických elektronových svazků a velkých proudů iontových svazků. Experimentální uspořádání spolu s jeho přesně definovanými částmi je prvním krokem k dosažení co nejlepších výsledků. Trajektorie svazků nabitých částic mohou být zakřiveny působením statických elektrických a magnetických polí a dále detekovány správně kalibrovanou měřící aparaturou. Jedna z možností měření energie iontového svazku je metoda měření doby letu, jež může poskytnout i informaci o intenzitě svazku. Urychlovače částic založené na interakcích laseru s plazmatem mohou nalézt využití v mnoha vědeckých, průmyslových a společenských oblastech.

Klíčová slova: laser, plazma, urychlovače částic, elektronové a iontové svazky, diagnostika částic velkých energií

Contents

Introduction

It is known that visible matter in the universe is mostly in the state of plasma. All stars, their cores and atmospheres, the interstellar hydrogen, the galactic nebulas are in this ionized state. In our solar system plasma can be found not only in the Sun but also in the solar wind and in the Van Allen radiation belt around the planets. On Earth matter in plasma state can be found in nature only in special phenomena as aurora borealis. In ordinary life plasma is found as an ionized gas in the cathode tubes used for various applications. Using plasma processes semiconductors are manufactured and used in microelectronic industry. High density plasma is generated in astrophysics laboratory to study hot and dense matter in order to reproduce the physical conditions inside the stars.

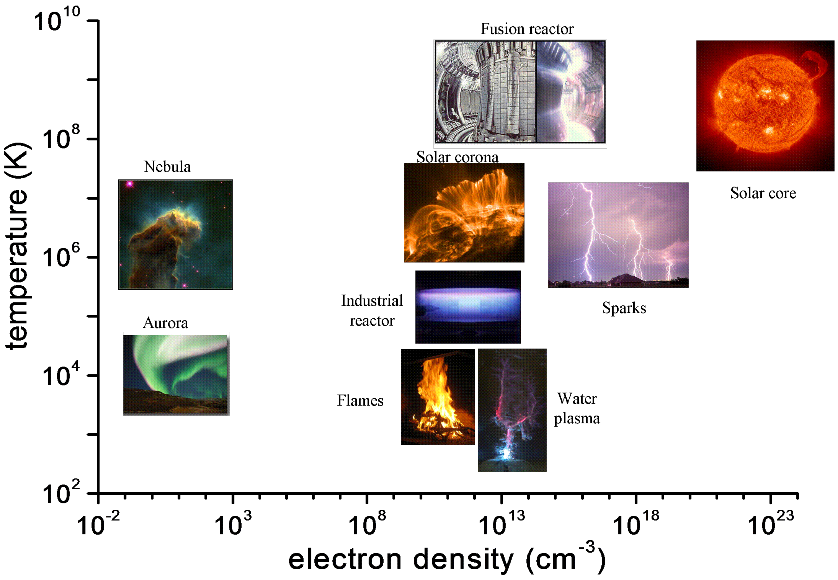

Figure 1: Plasma state of matter in nature is divided by its temperature and density.

Plasma is attractive as a potential source of energy produced from thermonuclear fusion. There are two leading concepts of fusion - magnetic confinement and inertial confinement. Inertial confinement fusion (ICF) has the leading project at National Ignition Facility in USA where 192 giant intense laser beams will be focused on a target filled with hydrogen fuel. A similar project is planned in Europe - the High Power laser Energy Research (HiPER) facility intended for demonstrating the feasibility of laser driven fusion. France military project at Laser Mégajoule is also concerned on ICF research but it is primary focused on France's own nuclear weapons industry. New European project dedicated to study the laser-matter interaction with ultra-relativistic laser intensities is the Extreme Light Infrastructure (ELI) project producing extreme power from attosecond-scale pulses.

The capability of ELI laser facility will open the way towards new particle acceleration techniques never investigated so far. In particular, these extreme power density lasers will explore new horizons for electron and ion stream acceleration in terms of beam energy, charge and quality, in order to replace the classic large-scale acceleration systems.

Chapter 1

Laser Plasma Accelerators

1.1 Basic plasma concepts

Plasma is a quasi-neutral system of charged and neutral particles which responds to electromagnetic fields with a collective behaviour. Quasi-neutrality means an approximated equilibrium between the positively charged ions and negatively charged electrons in plasma which dimension is much larger than a proper distance called Debye length. The presence of charged particles in plasma creates electric charge and electrostatic field which cause the forces influencing other charged particles. This results in compensation of the fluctuation in charge density and plasma appears as electrically neutral at large scales.

1.1.1 Debye Length

A basic characteristic of the plasma behaviour is to shield electric potentials placed in the plasma. When we put a charged particle in the plasma, it starts to attract the particles with the opposite charge and repulse the particles with the same charge. The placed particle will be surrounded by the particles with the opposite charge and the electrostatic potential will be shielded. In a case of the cold plasma the shielding would be perfect and no potential would be observed at scales larger than a distance called Debye length. But the temperature in plasma is finite. Thus there exists an edge of the cloud surrounding the placed particle where electric field is weak and particles on the edge have a sufficient thermal energy to escape from the electrostatic potential pit. Then the edge of the cloud is the radius on which the potential energy is in equilibrium with the thermal energy k_BT of the particles and the shielding is not perfect (k_B is the Boltzmann constant and T is the temperature). k_BT/e sized potential can penetrate into the plasma and causes a finite electric field. The Debye length is defined as [1]:

$$\lambda_D = \sqrt{\frac{\epsilon_0 k_B T}{n_e e^2}} \tag{1.1}$$

where T is expressed in K and n_e is expressed in m^{-3}. For the temperature 1 keV (1 eV = 11600 K) and electron density 10^{18} cm^{-3} the Debye length is $\lambda_D = 0.2$ μm.

The Debye length is the measure of the shielding distance. If the plasma size L is much larger than the Debye length it means that when there is any local concentration of the charge or when the outer potential is set inside the plasma system, it is shielded in short scales in comparison with L and leaves the rest of the plasma without any large potentials or electric fields.

In this definition of Debye length the temperature T is the electron one because the shielding is mostly provided by electrons, their motion is higher than the motion of ions

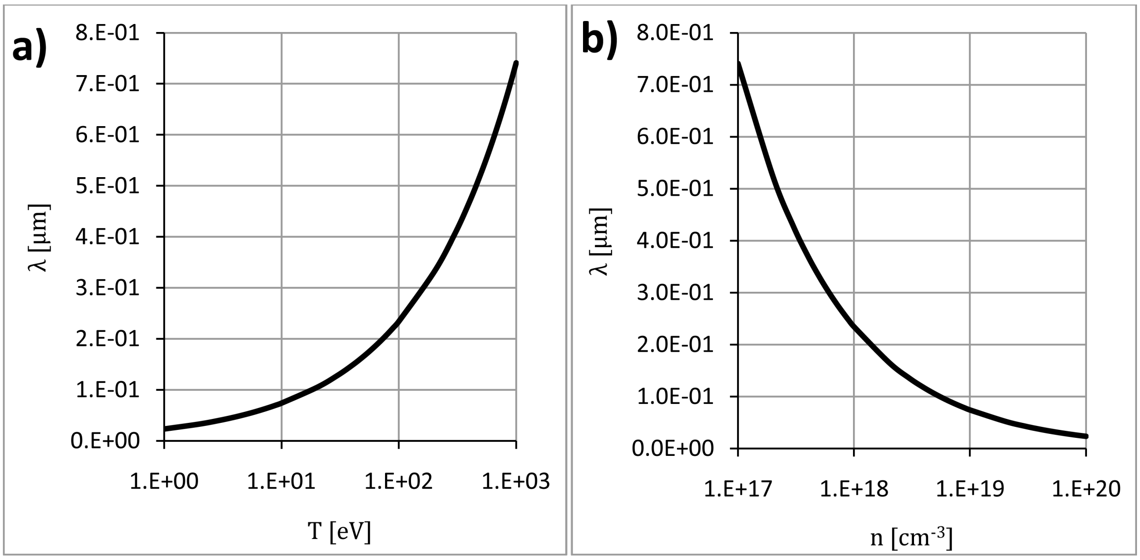

Figure 1.1: Characteristic of the Debye length as a function of a) temperature (logarithmic scale) at a constant value of $n = 10^{17}$ cm^{-3}, b) plasma density (logarithmic scale) at a constant value of $T = 1$ keV.

according to their mass. In case of an excess of negative charge, electrons will be repulsed leaving the heavier ions behind and shielding the charge. When there is an excess of positive charge electrons will be attracted surrounding them.

The mechanism of the Debye shielding occurs when there is a sufficient number of particles. The number of particles in Debye sphere can be calculated as [1]:

$$N_D = n_e \frac{4}{3} \pi {\lambda_D}^3 \cong 1.36 \times 10^6 T^{\frac{3}{2}} {n_e}^{-\frac{1}{2}}. \tag{1.2}$$

where temperature T is expressed in K and electron density n_e is in m^{-3}. For previously calculated Debye length and density and temperature mentioned, above the number of particles in Debye sphere will be $N_D = 5.4 \times 10^4$.

1.1.2 Saha Equation

The degree of ionization of the gas in thermal equilibrium is described by the Saha equation that can be approximately expressed as [1]:

$$\frac{n_i}{n_n} \approx 2.4 \times 10^{21} \frac{T^{\frac{3}{2}}}{n_i} e^{-\frac{U_i}{k_B T}} \tag{1.3}$$

with the assumption of $n_i/(n_n + n_i) \approx \; n_i/n_n$ where n_i is the ion density and n_n is the density of neutral particles. U_i is the ionization energy of the gas - the energy that one electron needs to be separated from the atom. E.g. hydrogen has ionization energy $U_i = 13.6$ eV, considering a temperature of 1 eV and an ion density of 10^{18} cm^{-3}, the ionization degree is $n_i/n_n = 3.7 \times 10{-}3$. Thermal energy of the gas is not uniformly distributed to all particles. The atom is ionized when collision with sufficient energy occurs. The increase of temperature makes n_i greater than n_n. Thus, plasma becomes fully ionized. Recombination depends on electron density inside the plasma.

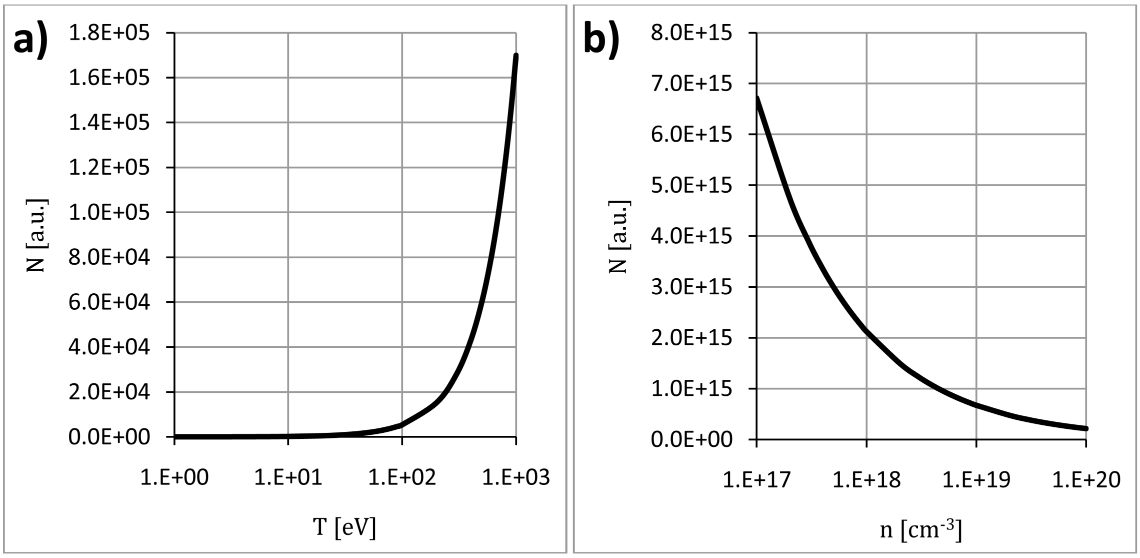

Figure 1.2: Characteristic of the number of particles in the Debye sphere as a function of a) temperature (logarithmic scale) at a constant value of $n = 10^{17}$ cm^{-3}, b) plasma density (logarithmic scale) at a constant value of $T = 1$ keV.

1.1.3 Vlasov equation and its momentum

The collective behaviour and a variety of laser-plasma interactions can be derived from the Vlasov equation and its moments, the fluid-like equations for electrons and ions, by averaging over the velocities. For the evolution of a collisionless plasma there is a phase space distribution function $f_j\left(x\left(t\right), v\left(t\right), t\right)$. This function presents the number of particles of a species j per unit of volume of the phase space as a function of time. Neglecting ionisation and recombination, the distribution function remains constant - the phase space density is conserved following a dynamical trajectory [2]:

$$\frac{df_j}{dt} = \frac{\partial f_j}{\partial t} + \dot{\mathbf{x}}\frac{\partial f_j}{\partial x} + \ddot{\mathbf{x}}\frac{\partial f_j}{\partial x} = 0. \tag{1.4}$$

From the laws of motions, the time derivative of x is the velocity v

$$\dot{\mathbf{x}} = v \tag{1.5}$$

and the second time derivative of x can be expressed from the Lorentz force:

$$m_j\ddot{\mathbf{x}} = q_j\left(\mathbf{E} + \mathbf{v}\times\mathbf{B}\right). \tag{1.6}$$

where q_j and m_j are the charge and mass of the jth particle and $\mathbf{E}$ and $\mathbf{B}$ are the electric field intensity and magnetic induction associated with the collective behaviour. Substituting from equations 1.5 and 1.6 into 1.4 the Vlasov equation for collisionless plasma will be:

$$\frac{\partial f_j}{\partial t} + \mathbf{v}\frac{\partial f_j}{\partial x} + \frac{q_j}{m_j}\left(\mathbf{E} + \mathbf{v}\times\mathbf{B}\right) = 0. \tag{1.7}$$

Vlasov equation along with the Maxwell's equations makes a complete behaviour description for collisionless plasma. Maxwell's equations for charged particles in vacuum are:

$$div\mathbf{E} = \frac{\rho}{\epsilon_0} \tag{1.8}$$

$$div\mathbf{B} = 0 \tag{1.9}$$

$$rot\mathbf{E} = -\frac{\partial \mathbf{B}}{\partial t} \tag{1.10}$$

$$rot\mathbf{B} = \mu_0 \mathbf{j} + \epsilon_0 \mu_0 \frac{\partial \mathbf{E}}{\partial t} \tag{1.11}$$

where ρ is the charge density and $\mathbf{j}$ is the current density.

Equations for the evolution of the density in space and time can be derived from the velocity moments of the Vlasov equation. The zero moment of the Vlasov equation (averaging over the velocities) gives the continuity equation for the particle density:

$$\frac{\partial n}{\partial t} + div\,(nu) = 0 \tag{1.12}$$

where u is the mean velocity and a product nu is the particle flux. The particle flux can be also determined from the first moment of the distribution function f_j. Equation 1.12 represents the conservation of the number of particles.

To derive the first moment, it is necessary to multiply the Vlasov equation by momentum and average it over the velocity as:

$$\int mv \frac{df_j}{dt} dv = 0. \tag{1.13}$$

The solution of this integral gives the momentum conservation law (Navier-Stokes equation)

$$\frac{\partial u}{\partial t} + (u\ grad)\,u = -\frac{1}{\rho} div\mathbf{P} + \frac{q}{m}\left(\mathbf{E} + \mathbf{v} \times \mathbf{B}\right) \tag{1.14}$$

where $\rho = mn$ is density and $\mathbf{P}$ is pressure tensor, which can be determined from the second moment of the distribution function f_j. Components of the pressure tensor determine motion direction and the momentum component:

$$P_{ij} = mn \left\langle v_i v_j \right\rangle . \tag{1.15}$$

In an isotropic plasma, the pressure tensor consists of diagonal dyad of a magnitude p. Plasma can also have two temperatures in presence of magnetic field. In this case there exist two kind of pressure, $p_{\|} = nk_B T_{\|}$ and $p_{\perp} = nk_B T_{\perp}$. First two diagonal components will be $p_{\perp}$ and the third diagonal component $p_{\|}$ is in the direction of the magnetic field. In an ordinary liquid there are also the non-diagonal components presenting the viscosity.

For plasma composed of electrons and one single ion species, equations 1.12 and 1.14 constitute the two-fluid model. This description is completed by Maxwell's equations 1.8 – 1.11 which relate the electric and magnetic fields to the charge and current densities of the plasma. There can be also used a one-fluid model where the matter density and mean velocity is used, but the temperature of the fluid may differ in terms of ion and electron one. The two-temperature one-fluid hydrodynamics is widely used for description of laser-plasma interaction by using quasi-neutrality of the plasma.

1.1.4 Plasma interactions with electromagnetic waves

An interesting plasma behaviour is its interaction with the electromagnetic waves. We will make the assumption of transverse waves in the form:

$$\mathbf{E} = \mathbf{E_0 e^{i(k \cdot x - \omega t)}} \tag{1.16}$$

where $\mathbf{k}$ is the wave vector, ω is frequency of the wave, $\mathbf{x}$ and t are coordinates in space and time. The Maxwell's equations for electromagnetic waves in vacuum are:

$$div\mathbf{E} = 0 \tag{1.17}$$

$$div\mathbf{B} = 0 \tag{1.18}$$

$$rot\mathbf{E} = -\frac{\partial \mathbf{B}}{\partial t} \tag{1.19}$$

$$rot\mathbf{B} = \epsilon_0 \mu_0 \frac{\partial \mathbf{E}}{\partial t}. \tag{1.20}$$

Using equation 1.20 and applying the operator rot in 1.19, under the assumption 1.16 and considering the equation 1.17, the propagation of the light wave in vacuum will follow the equation:

$$\Delta \mathbf{E} = \epsilon_0 \mu_0 \frac{\partial^2 \mathbf{E}}{\partial t^2}. \tag{1.21}$$

resulting in disperse relation

$$k^2 = \omega^2 \epsilon_0 \mu_0 \Rightarrow c^2 k^2 = \omega^2. \tag{1.22}$$

where ω/k is the phase velocity of the light. For electromagnetic waves propagating in plasma it has to be considered the Maxwell's equations 1.8 − 1.11 and for transverse waves equation 1.17 where the light wave will follow the modified equation:

$$\Delta \mathbf{E} + \epsilon \mu \frac{\partial^2 \mathbf{E}}{\partial t^2} = \mu \frac{d\mathbf{j}}{dt}. \tag{1.23}$$

Considering the latter equation, under the assumption 1.16, the light waves or microwaves frequency will be high and we can then consider only the electron motion and express the current density as:

$$\mathbf{j} = -n_e e \mathbf{v_e} \tag{1.24}$$

and integrating the Lorentz force (neglecting the magnetic field) in the form:

$$m \frac{\partial \mathbf{v_e}}{\partial t} = -e\mathbf{E} \tag{1.25}$$

and substituting electron velocity $\mathbf{v_e}$ into equation 1.24, the equation 1.23 can be figured resulting in a dispersion relation of the propagating electromagnetic wave in the plasma with frequency [3]:

$$\omega_p^2 = \frac{n_e e^2}{\epsilon_0 m} \tag{1.26}$$

This is called plasma frequency and for electron density $n_0 = 10^{18}$ cm^{-3} it is $\omega_p = 5.7 \times 10^{13}$ s^{-1}. The following relation is also valid:

$$\omega^2 = \omega_p^2 + c^2 k^2 \tag{1.27}$$

Thus, if the plasma frequency is higher than laser frequency, the electromagnetic wave will not propagate into the plasma. If plasma frequency tends to the laser frequency, the total reflection occurs. To reach the total reflection, from equation 1.26 the plasma density (the critical density) can be estimated for the required laser frequency ω_L, where plasma frequency in eq. 1.26 is substituted by laser frequency. It is called critical density, n_C, and can be expressed as follow:

$$n_C = \epsilon_0 m \frac{\omega_L^2}{e^2}. \tag{1.28}$$

From equation 1.25 the phase velocity v_φ and the group velocity v_g are [1]:

$$v_\varphi = \frac{\omega}{|\mathbf{k}|} = \sqrt{c^2 + \frac{\omega_L^2}{k^2}}, v_g = \frac{d\omega}{dk} = \frac{c^2}{v_\varphi} \tag{1.29}$$

It is seen from eq. 1.26 that the phase velocity is bigger than the speed of light whereas the group velocity is less than the speed of light in vacuum. For a magnitude of wave number $|k| = 10^6$ m^{-1} and electron density $n_e = 10^{18}$ cm^{-3} the phase velocity is $v_\varphi = 3.05 \times 10^8$ ms^{-1}, and the group velocity is $v_g = 2.95 \times 10^8$ ms^{-1}.

1.1.5 Ponderomotive force

In laser-plasma interactions the light interacts with the plasma primarily via a ponderomotive force. It is a non-linear force proportional to the gradient of the laser intensity [4]:

$$\mathbf{F_P} = -\frac{e^2}{4m\omega^2} \nabla \mathbf{E^2} \propto \nabla I \tag{1.30}$$

where ω is the laser frequency.

The ponderomotive force affects electrons to oscillate in the direction of the electric field $\mathbf{E}$, the velocity have the same direction as the electric field, whereas the magnetic field shift their orbits. The magnetic part of the Lorentz equation 1.6 pushes electrons in the way of $\mathbf{k}$ ($\mathbf{E}$ has the same direction as $\mathbf{k}$). Averaging the phase of vectors $\mathbf{v}$ and $\mathbf{B}$ over one oscillation period will result in a drift motion in the way of $\mathbf{k}$. If the amplitude of the wave is changing, the electrons will accumulate in areas of the low amplitude. The ponderomotive force affects mostly electrons but this force is then transferred to ions. When the accumulation of electron is complete by affecting the ponderomotive force, an electric field $\mathbf{E_s}$ is created due to the separation between electrons and ions, thus the total force affecting one electron is:

$$\mathbf{F_e} = -e\mathbf{E_s} + \mathbf{F_P} \tag{1.31}$$

The ponderomotive force affecting ions is much lower than the one for electrons. The total force affecting the ion is approximately

$$\mathbf{F_i} = e\mathbf{E_s} \tag{1.32}$$

As a result the ponderomotive force pushes plasma from the regions where the laser high field intensity is present and makes a density gradient initiating the pressure gradient.

1.1.6 Self-focusing

One of the consequence of the ponderomotive force is the self-focusing of the laser beam inside the plasma. The ponderomotive force pushes plasma electrons out of the beam, leaving plasma frequency ω_p lower and dielectric constant higher than outside of the beam. According to these attributions plasma has the same effect as a convex lens focusing the beam on a small diameter. The self/focusing power treshold formula is [4]:

$$P_{cr} = 17\left(\frac{\omega^2}{\omega_p^2}\right)[GW] \tag{1.33}$$

where ω is laser frequency and ω_p is plasma frequency.

1.2 Basic principles of laser-driven plasma-based particle acceleration

1.2.1 Electron acceleration mechanism

As the ultra-short laser pulse propagates through the plasma, the ponderomotive force separates electrons from ions and makes a travelling electric field. The electric field travels with a phase velocity close to the speed of light necessary for particle acceleration. The laser leaves a potential wake inside the plasma, for this reason this principle is known as laser wakefield acceleration (LWA). This phenomenon can be considered similar to the wake produced by a boat sailing on a lake, leaving a wave in its wake.

The longitudinal electric field responsible for acceleration is [3]:

$$E_L = m_e c \frac{\omega_p}{e} \tag{1.34}$$

E.g. for a plasma with electron density 10^{18} cm^{-3} the electric field reaches 100 GV/m.

If electrons are injected near the peak of the wave, they can be accelerated in the plasma wake potential. It is similar to the surfer who is trapped and accelerated in an ocean wave. The electrons are surfing down the potential wave gaining a kinetic energy and at the bottom of the wake potential the electron bunch will be quasi-monoenergetic. Plasma wavelength is defined as [5]:

$$\lambda_p = 2\pi \frac{c}{\omega_p} \tag{1.35}$$

There are several ways how to inject electrons with a sufficient initial energy (to be trapped and accelerated). Widely is used only a single laser pulse, which drive the wakefield to extremely high amplitudes in a very nonlinear regime. It leads to the formation of an electron-evacuated cavity (the bubble), filled with ions and surrounded by a dense wall of electrons. When the electron density at the walls reaches a threshold value, self-injection occurs and electrons are injected at the back of the bubble. Injection stops when the charge density of the trapped electron bunch is comparable to the charge density at the bubble walls. Thus the quasi-monoenergetic electron bunch is formed. Self-injection depends on the nonlinear evolution of the laser pulse. This regime is called Bubble regime. The acceleration occurs in millimetre distances, electron bunches have relatively low energy spread (5–10%) and charge of hundreds of pC [6, 7].

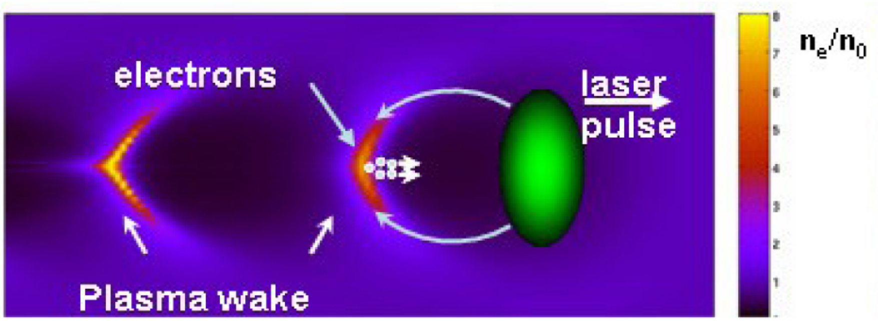

Figure 1.3: Scheme of injection mechanism in the bubble regime. Electrons are injected from the bubble walls at the back side and accelerated at the plasma wake potential.

1.2.2 Ion acceleration mechanism

Efficient generation of ion beams is observed due to the interaction of high power laser pulses with solid targets. We will describe two different regimes of laser-driven ion acceleration. In both regimes, the laser beam is focused onto a solid target producing a hot ionized plasma. The plasma emits neutral particles, electrons and ions but also UV and X radiation.

Target normal sheath acceleration

The first regime is the target normal sheath acceleration (TNSA) where an ultra-intense short laser pulse is focused onto the front surface of a thin solid target producing plasma and fast electrons [8]. Varying laser intensities from 10^{17} W/cm^2 to 10^{20} W/cm^2 the electrons reach temperatures from 10 keV to 10 MeV. Electrons penetrate through the solid target and at the rear surface they form a Debye sheath effecting as a virtual cathode where the induced electric field is:

$$E_{in} = T/e\lambda_D \tag{1.36}$$

for $\lambda_{De} = 1$ μm and the mentioned laser intensities of 10^{17} W/cm^2 to 10^{20} W/cm^2 and temperatures of 10 keV to 10 MeV, as mentioned above, the induced field is $10^{10} - 10^{13}$ V/m. This electric field ionizes atoms at the rear surface of the target and accelerates them. Assuming an acceleration distance (L_a) of 10 μm, the ion energy for a certain charge state z is defined as:

$$\epsilon = zeL_aE_{in} \tag{1.37}$$

and for the mentioned parameters and for the charge state $z = 1$ the ions can gain energies from 0.1 MeV to 100 MeV. These ions are accelerated mostly in the direction perpendicular to the target layer, for this reason the angular divergence of the beam is mostly less than 20° [8]. The front layer consists of a material with high electron density, and the rear layer consists of a hydrogen-rich material, usually metal-hydrogen. The front layer acts as a source of fast electrons and the rear surface acts as a source of hydrogen ions, which are accelerated in the way described above.

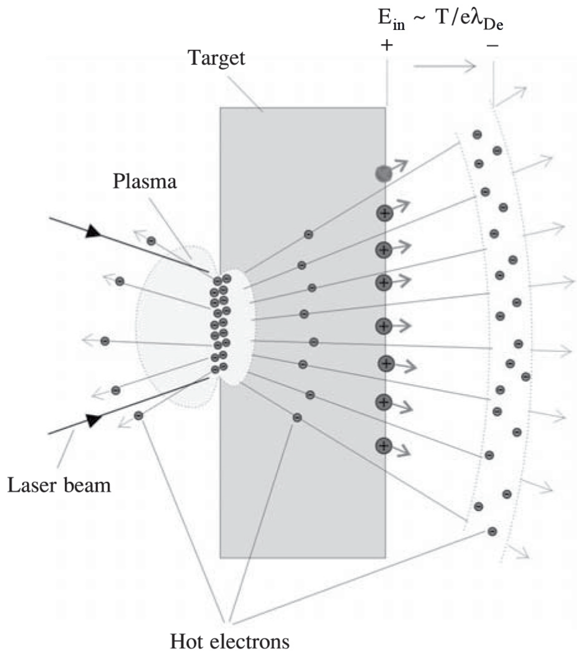

Figure 1.4: Scheme of the TNSA method. Formed virtual electron cathode at the rear side of the target induces electric field responsible for ion acceleration.

The curved target (e.g. spherical target), or generally shaped target, can be used for increasing the current density of the proton beam. The ion-plasma beam can be focused as a result of the laser focal spot focusing, thus it can be very small (tens of microns). On the contrary, in a conventional radio-frequency accelerator the ion beam focusing is limited by the Coulomb interaction between ions.

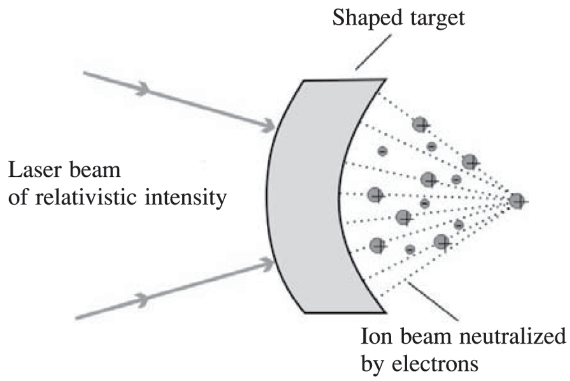

Figure 1.5: Scheme of the shaped target at TNSA method. The generated plasma beam is focused due to the normal acceleration direction on the rear side of the target.

Skin-layer ponderomotive acceleration

The second regime is the skin-layer ponderomotive acceleration (SLPA) where light ions are generated. In this regime mainly plastic thick targets are used. The pre-pulse of the laser beam ionizes the front side of the target creating a preplasma layer - the skin-layer, which thickness have to be much less than the focal spot diameter of the laser [8]. The laser prepulse intensity has to be significantly lower than the main laser pulse. This condition is much harder attainable for relativistic laser intensities. The main laser pulse interacts intensively with the skin-layer near the surface at the critical electron density and the geometry of the interaction is almost planar. The high plasma density gradient in the interaction region induces two opposite ponderomotive forces which break the plasma and drive two thin plasma blocks towards the vacuum and the plasma interior, respectively [8]. The current density of ions accelerated in the backward dirrection can be very high. The angular divergence of the ion beam is small due to the almost planar acceleration geometry. In order to reach ion energies in the MeV range, relativistic laser intensities have to be used.

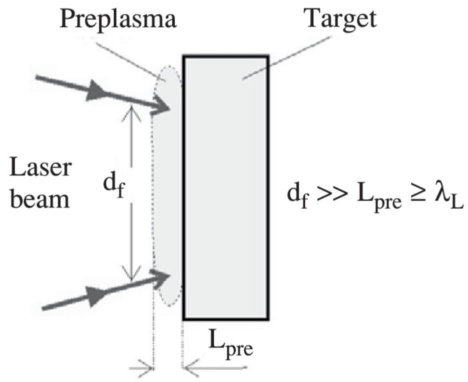

Figure 1.6: Scheme of the SLPA method. The foot of the laser beam generates a plasma skin-layer of thickness L_{pre} which is broken due to the induced ponderomotive forces and accelerated in the backward direction.

By means of the TNSA method, using relativistic laser intensities and high laser energies, proton beams with currents comparable to the subrelativistic SLPA method can also be produced. In other words, at the same laser intensity, the produced proton current density is much higher for SLPA than for TNSA. Proton density at the source is about thousand times higher in SLPA than in TNSA.

The main problems concerning the generation of heavy ions are related to the ionization efficiency of high charge state ions, and to the acceleration of these ions without any loss of charge state due to recombination effects. The basic principle of atom ionisation is the collisional ionisation caused by inelastic collisions of free electrons which were previously accelerated by the interaction with the laser pulse. If the medium is dense enough, the ionization will be more efficient. This mechanism of producing highly charged ions is more attainable in the case of the short pulses, providing higher laser intensities than for the long pulse ones. However, it is more difficult to obtain highly charged ions far from the expansion zone because of the short interaction time of the short-pulses with the plasma and the consequent rapid adiabatic cooling of the produced plasma with electron-ion recombination.

The SLPA mechanism with double-layer effect in expanding plasma can be used for long laser pulses. The fast electrons come from one layer in front of the expanding plasma and cause the ion acceleration, accelerating first the ions of the highest charge state according to the highest z/A ratio (the charge state over the mass number of the atom) [8]. When the TNSA mechanism is used the laser intensity has to be greater than 10^{19} W/cm^2 because the electric field produced by the fast electrons has to be high in order to obtain high charge states at the rear surface [8].

1.3 Brief history

The first idea of using laser-plasma interactions to accelerate particles dates back to 1979, when Tajima and Dawson published a paper in Physical Review Letters about laser electron acceleration [9]. They proposed a simple mechanism in which the laser beam is injected into the underdense plasma (plasma density is less than the critical one) and excites (via the ponderomotive force) an electrostatic wake behind the laser beam. Electrons can be trapped in this wake and then accelerated to high energies. They demonstrated this acceleration mechanism through computer simulations. Using simulations the processes of laser-plasma interactions were understood and many simulations were performed to decide the experimental setup as the plasma density and laser intensity.

As already reported, the electric field in plasma wake is caused by the ponderomotive force which is proportional to the gradient of the laser intensity. To obtain higher forces causing higher electric fields (and better acceleration of the particles) the laser intensity has to be increased. The intensity increase is much more difficult for the long laser pulses, thus the short laser pulses (at picoseconds or subps scales) needed to be developed. The new laser technology based on the chirped pulse amplification (CPA) was developed. The CPA device generates ultrashort, ultra-high-intensity pulses with duration from 20 to 100 femtosecondes. Using a short pulse a high intensity gradient is produced which means strong ponderomotive force. When the laser pulse reaches a relativistic intensity it generates the plasma wave via ponderomotive force and accelerates particles at relativistic velocities.

Many experiments proving the laser electron acceleration mechanism theoretically studied were performed in the 90's [10, 11, 12, 13]. These experiments were aimed to the observation of high energy electron bunches (few MeV) accelerated by the laser wakefield mechanism, however, at the begining the produced electron beams were far from the quasi-monoenergetic streams produced by classical accelerators.

In the past few years various experiments were performed by using laser systems based on CPA technique, where the accelerated electrons reached hundreds of MeV and even more than GeV energies [5, 6, 7, 14, 15, 16]. Usually supersonic helium gas-jet is used for generation of the underdense plasma medium. The laser beam is focused above the gas-jet nozzle and the laser pre-pulse ionizes the gas whereas the main pulse interacts only with the plasma. The whole ionization process does not play a role in the laser-plasma interaction.

At Rutherford Appleton Laboratory using Ti:Sapphire laser system there were produced electron beams up to hundred MeV with a beam divergence less than 5° [5]. Using a high laser power with controlled plasma density a monoenergetic structure with a narrow peak in the spectrum was observed at 70 MeV energy with a full-width at half-maximum (FWHM) energy spread less than 3%. No monoenergetic electrons were observed under a certain electron density [5].

In France at Laboratoire d'Optique Appliquée an experiment was performed by using one joule laser energy (Ti:Sapph based on CPA) [14]. They generated 170 MeV electron beam, which were highly collimated and quasi-monoenergetic. They observed also 10% energy conversion between laser beam and electrons. Their conclusion from the experimental results was that the use of laser pulses shorter than the plasma period:

$$\tau = 2\pi/\omega_p \tag{1.38}$$

is beneficial for high-quality and monoenergetic electron acceleration.

In Korea at the Advanced Photonics Research Institute an experiment was realized in order to demonstrate the simplest GeV-class accelerator by the self-guided laser wakefield acceleration method [16]. There were used two gas-jet nozzles 4 mm and 10 mm long. In the longer gas-jet two main peaks were observed , one with high-charge and energy of about 330 MeV and another with low-charge and energy of about 540 MeV. The maximum electron energy reached was over 1 GeV. In 4 mm gas-jet the low-charge electron bunches with the energy greater than 1 GeV were clearly observed. Rise in the plasma density caused a dephase of the GeV bunch to 900 MeV.

In Los Alamos National Laboratory it was performed an experiment of accelerating Palladium and Carbon ions using neodymium-glass laser (based on CPA) and TNSA double-layer acceleration method [17]. Heating the target to temperatures higher than 1100 K, complete dehydrogenization was performed and carbon compounds formed very thin graphite layer at the monolayer scale on the surface of the palladium foil of thickness 20 μm. The graphite layer was used as the rear side of the target. Acceleration of C^{5+} and C^{6+} ions and also Pd^{22+} ions (which are the next highest charge-to-mass ratio ions) was observed. According to the highest charge-to-mass ratio the C^{5+} ions were dominantly accelerated and had a monoenergetic distribution with a mean energy of 36 MeV, whereas Pd ions had a typical exponential spectrum.

At the University of Jena an experiment using JETI Ti:Sapph laser (based on CPA) and TNSA double-layer acceleration method was performed [18]. The solid target was a 5 μm thin titanium foil (thinner foil would result in higher proton energies but according to reproducibility of the experiment the thicker target was chosen). On the rear side of the foil there were dots made of polymethylmethacrylate (PMMA). This hydrogen-rich PMMA dots were constructed by the femtosecond laser ablation and they were made only for one single shot. The laser pulse hitting the target exactly on the opposite side of the PMMA dots, generated a peak of proton energy at 1.2 MeV. It is expected, that gold target could deliver more hot electrons to be used for accelerating protons.

1.4 Recent advances

Recently, alternative methods for electron injection in the wakefield have been tested. For the production of monoenergetic electron bunches it is required that the injected beam load have a duration shorter than $\lambda_p/c = 30 - 100$ fs (for electron densities in the range $1.2 \times 10^{18} - 1.4 \times 10^{19}$ cm^{-3}) where λ_p is the plasma wavelength and c is the speed of light. The production of such short bunches is hardly attainable by conventional radio-frequency accelerators, in fact no successful experiment with the external radio-frequency injector was demonstrated.

1.4.1 Colliding pulses

Second laser pulse may be used for stabilization of the electron beam. The principle of using second pulse with the same central wavelength and the same polarization is that the first laser pulse creates a wakefield and the second pulse is used for electron injection [7]. The collision of the pulses and their interference create a laser beatwave pattern inside the plasma. The beatwave pattern is a standing wave, with characteristic spatial scale $\lambda/2$ where λ is the laser central wavelength and the phase velocity close to the zero. The ponderomotive force of the beatwave is large and it traps electrons and accelerates them at MeV energies. Some of these electrons can gain sufficient energy to be trapped in the wakefield driven by the first laser pulse and then be accelerated to relativistic energies.

This regime is more complicated to be experimentally realized, otherwise it permits to control easily the electron beam parameters (e.g. charge of the beam and its energy spread) can be controlled.

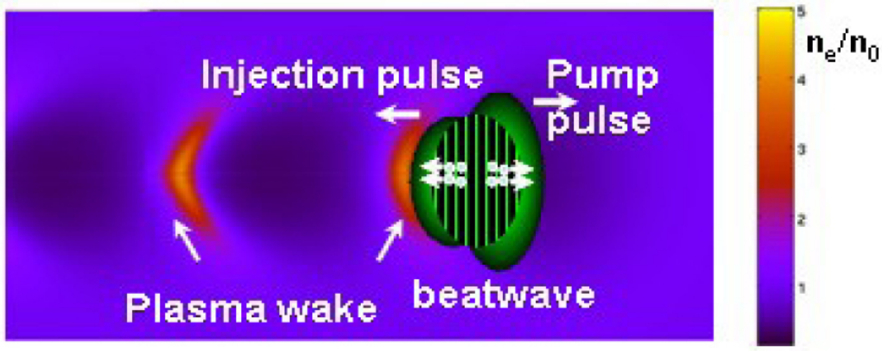

Figure 1.7: Scheme of injection mechanism in the colliding laser pulses regime. Electrons can be injected by the second laser pulse in the wakefield of the first pulse and further accelerated.

This particular experiment, i.e. colliding of two laser pulses inside the plasma, was performed at Laboratoire d'Optique Appliquée for the first time and highly collimated electron bunches were produced [19]. The differences between the "self-injection" regime and "colliding laser pulses" regime were studied. The main difference was that at the self-injection regime electron beams with energies around 100 MeV and relatively large energy spread were observed, whereas, at the colliding pulses regime, quasi-monoenergetic bunches around 200 MeV energies and with narrow energy spread, were clearly observed in similar laser conditions. Every shot at the colliding regime consistently gave small statistical deviations in the monoenergetic part of the electron distribution when using a parallel polarization of the two laser pulses. When the polarization of the pulses was orthogonal, no monoenergetic electron beam was observed. This method is promising for further increasing of the electron beam charge up to nanocoulomb level and increasing the electron energy up to GeV scales, by using waveguides.

1.4.2 Capillary discharge waveguide

The wake has a phase velocity lower than the speed of light in vacuum, therefore the phase slippage may occur between relativistic particles and the wake. The linear dephasing (to dephase means to put out of phase, as two parts of a single alternating current) length L_d over which electrons outrun the wake and slip into the decelerating phase, limits the distance over which acceleration occurs.

$$L_d = \frac{\lambda_p^3}{\lambda^2} \propto n_p^{-\frac{3}{2}} \tag{1.39}$$

where λ_p is the plasma wavelength, λ is the laser wavelength and n_p is plasma density. It was proved in experiments that accelerating at the L_d length lead to the production of low energy-spread electron beams [15].

At Lawrence Berkley National Laboratory an experiment where the gas-jet was replaced by a gas-filled capillary discharge waveguide was performed [15]. The capillary discharge waveguide was used to guide laser pulses of relativistic intensities by means of low plasma densities and, as a consequence, long dephasing lengths. The ionization in the plasma is efficient even at very low gas densities. Hydrogen gas was filled inside the capillary and it was ionized by a discharge between electrodes at the capillary ends. Quasi-monoenergetic structures were observed at two capillaries with a similar plasma density (both capillaries were long hundreds of μm). The dimension of the capillary can be set in accordance with the dephasing length L_d. The experiment with shorter capillary showed a quasi-monoenergetic electron bunch with about 0.5 GeV energy. By using the longer capillary, a first quasi-monoenergetic bunch at 0.8 GeV and a second one at 1 GeV, were observed. The sub-GeV bunch was also predicted in numerical simulations: it is explained by assuming that the second electron bunch is trapped and accelerated "in a wake bucket behind the first" electron bunch. The accelerated beam at 1 GeV is less stable than the one at 0.5 GeV. This new experimental configuration shows the possibility of realizing compact GeV accelerators driven by laser power on the order of tens of TW.

Chapter 2

Preparation of pilot experiments on particle acceleration at PALS facility

2.1 The 15 TW Ti:Sapphire laser at PALS

The experiment of laser-driven particle acceleration will be made at Prague Asterix Laser System (PALS) facility using the 15 TW Ti:Sapphire laser.

Figure 2.1: The COHERENT compact 15 TW Laser System.

The main parts of the laser system are: a Verdi oscillator pump laser, a Mira seed oscillator, a Ti:Sapphire chirped pulse amplifier and a pulse compressor, as sketched in figure 2.2. The output laser beam produces approximately 15 TW of laser power at central wavelength 800 nm in pulse duration less than 40 fs at a 10 Hz repetition rate. The table below reports technical specification of the laser system.

The laser system starts at Verdi diode-pumped solid-state green laser used for pumping the Mira seed oscillator. The seed oscillator works at 20 fs operation with the 800 nm output beam. The output beam of the seed is stretched to more than 200 ps in the Legend-USP femtosecond Stretcher which is pumped by a 10 mJ of the 1 kHz Evolution-15 pump laser. The stretched pulse is amplified to pulse energy of more than 2 mJ at 10 Hz. The uncompressed output is then directed into a single stage multi-pass Ti:Sapphire amplifier

Power	>15 TW
Repetition Rate	10 Hz
Pulse Energy (Pre Compression)	>700 mJ
Pulse Energy (Post Compression)	>550 mJ
Pulse Duration	<40 fs
Central wavelength	∼800 nm
Energy Stability	2,5% RMS (1 hr), <10% Drift (8 hrs)
Pointing Stability	5-10 μrads (short-term 500 shots)
Beam Size	76 mm (aperture <112 mm)
Beam Profile	Flat top
Polarization	100:1 Linear
Contrast (>1 ns)	>1.000:1 pre pulse (10^{6th} with additional hardware)

Table 2.1: TW Ti:Sapphire laser specifications.

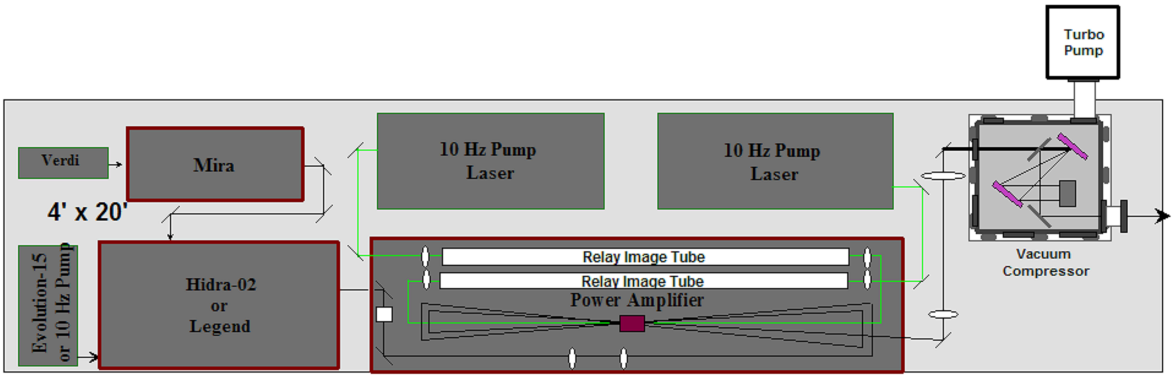

Figure 2.2: The layout of the laser system.

pumped by more than 2 J pump lasers at wavelength of 532 nm. The multi-pass output is compressed in a dual grating vacuum compressor to reach final pulse energy of more than 550 mJ, less than 40 fs at 10 Hz repetition rate [20].

The basic parameters usually used to describe a laser beam are: intensity, pulse energy, Rayleigh length and vector potential. For a given laser power P and laser beam section S the intensity is defined as:

$$I = \frac{P}{S} \tag{2.1}$$

also called laser power density. The laser energy for a given pulse length τ is:

$$E = P\tau \tag{2.2}$$

For example a 15 TW laser beam with pulse length 40 fs has pulse energy of 600 mJ.

The Rayleigh length is the distance from the location of the minimal beam radius (the focal spot radius) where the beam radius is increased by a factor of the square root of 2 (for a circular beam the distance where the mode area is doubled). For Gaussian beams the Rayleigh length is determined by the laser focal spot diameter (d) and wavelength [4]:

$$Z_R = \frac{\pi d^2}{4\lambda} \tag{2.3}$$

The Rayleigh length determines the focus depth. As it can be seen from equation 2.1, a weaker focusing (higher Z_R) reduces the intensity, whereas stronger focusing leads to a strong divergence, which limits the effective interaction length of the high intensity laser beam with a preformed plasma.

The potential vector of the laser beam is determined as [21]:

$$a_0 = 0.885 \times 10^{-9} I^{\frac{1}{2}} \left[W/cm^2\right] \lambda \left[\mu m\right]. \tag{2.4}$$

In the pilot experiment at PALS it is expected to focus the 15 TW laser beam onto different focal spot diameters. In a case of the focal spot diameter 15 μm the intensity will reach 8.5×10^{18} W/cm^2 having a Rayleigh length 221 μm. The vector potential of the laser beam will be $a_0 \sim 2$, permitting to work in the Bubble regime [3]. Focusing the laser beam onto 30 μm diameter will decrease intensity to 2.1×10^{18} W/cm^2 but the Rayleigh (and also the interaction) length will rise up to 884 μm. The potential vector in this case will be slightly less than the unit which is less convenient for particle acceleration as the ponderomotive potential is proportional to a_0^2. The higher is the potential vector, the stronger are the induced ponderomotive forces. In both cases an amplified spontaneous emission (ASE - a process where spontaneously emitted radiation is amplified) contrast will be greater than 10^5, this is the contrast between the main laser pulse beam intensity and the intensity of the radiation ahead and behind the pulse (the pedestal of the main pulse).

If electrons are accelerated in the LWA regime using intensities in the range $10^{18} < I < 10^{19}$ W/cm^2 and plasma density in the range $10^{18} < n_e < 10^{19}$ cm^{-3} (corresponding to plasma wavelengths $10.5 < \lambda_p < 33.3$ μm) the dephasing length, according to the equation 1.39, will be in the range $1.8 < L_d < 57.7$ mm. The assumption for the stable bubble regime is that the focal spot diameter must be greater than the pulse length ($c\tau$) and the plasma wavelength [3]. The pulse length will be less than 40 fs (less than 12 μm) which agrees with both above reported focal spot diameters, but the plasma wavelength gives the limitation to the plasma density which has to be higher than 1.3×10^{18} cm^{-3} and 5.0×10^{18} cm^{-3} for 30 μm and 15 μm focal spot diameter, respectively.

The self-focusing of the laser beam occurs for laser power greater than the critical power, as reported in equation 1.33.

For a density range $10^{18} < n_e < 10^{19}$ cm^{-3} the corresponding critical power is $3 < P_{cr} < 30$ TW. The 15 TW laser beam require the minimum electron density 2×10^{18} cm^{-3} to reach the self-focusing of the laser beam inside the plasma.

2.2 Relativistic electron streams

The design of the experimental setup for pilot experiments in the LWA - bubble regime is shown in figure 2.3. The incoming laser beam is reflected by a flat mirror (FM) onto an off-axis parabolic mirror (OAPM). Then the laser beam is focused above the nozzle reaching the maximum intensity inside the supersonic helium gas-jet injected from the nozzle. By the mechanism described in chapter 1.2.1 the quasi-monoenergetic bunch of electrons is generated and propagates along the same direction of the laser beam. The electron beam passes through a collimator, an integrating current transformer (ICT) and finally through a frame containing a permanent magnet. The magnetic field deflects the electrons to different angles according to the electron velocities. Then the electrons beam on their new trajectories hit the LANEX phosphorus screen producing a visible light at the impact region. The light coming from the LANEX is reflected by the FM and focused by the lens to an intensified charge-coupled device (ICCD) camera.

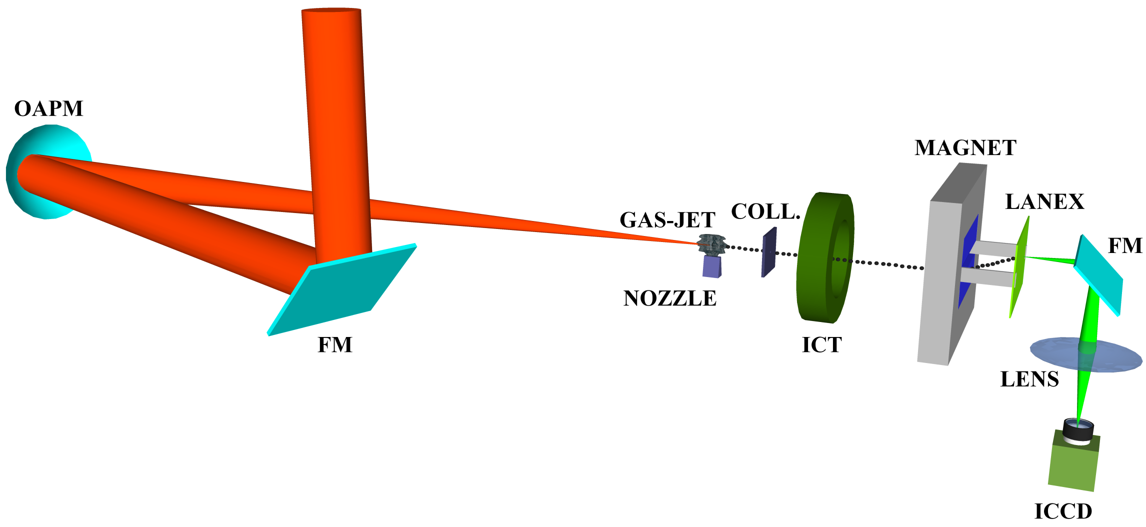

Figure 2.3: Scheme of the electron stream generation. An ultra-short and ultra-intense laser pulse is focused onto the supersonic gas-jet producing a high energy electron beam. The electron beam passes through collimator (coll.) and is measured by using the ICT, magnet, LANEX phosphorus screen, additional optics and ICCD camera.

The laser beam is focused onto the supersonic gas-jet by the OAPM. The OAPM is free from the spherical aberrations and focus the parallel beam to a small point which does not lie on the same axis as the original laser beam. The main parameter of the OAPM is the so-called f-number. The f-number (f/#) denotes the ratio of the focal length to the diameter of OAPM (smaller f/# provides larger diameter of the OAPM, reflecting greater amount of light generally). In electron acceleration experiments the advantage of a smaller f/# is the small energy spread in the electron distribution, whereas a higher f/# provides the generation of stable and high energy electron beams.

The laser-plasma interaction length depends on the size and shape of the nozzle of the gas-jet. It is expected to operate with a rectangular nozzles with lengths of 1 mm, 2 mm, 4 mm and width 1 mm. The density of the gas-jet can be tuned by varying the pressure inside the nozzle. To keep the density at the mentioned value till the laser pulse passes through, the velocity of the flowing gas has to be supersonic (it can reach even the Mach number of 5) because of the immediate expansion in the vacuum chamber which would lead to decrease density and the failure of the experiment. Widely is used a Laval nozzle for these experiments [16]. It is used as a means for accelerating the flow of the gas passing through it to supersonic velocities. It is expected for pressure range 0.5–2 MPa that the density of the gas-jet reaches 10^{19} cm^{-3}. Helium is used as the gas medium, mainly because it has heavier ions and provides more electrons than hydrogen.

As a collimator the stainless steel is used with a pinhole of 1 mm in diameter. The collimator improves the electron beam quality decreasing the spatial distribution and improving the resolution of the electron beam. It also protects the devices beyond the collimator from the radiation and electron streams generated in the plasma and propagating in the non-axis direction of the experimental setup which could cause the damage of the diagnostics systems.

The ICT is a capacitively shorted transformer and a fast read out transformer in a common magnetic circuit designed to measure the charge in a very short pulse with high accuracy [22]. This device is a linear integrator for high frequency spectrum typical for a

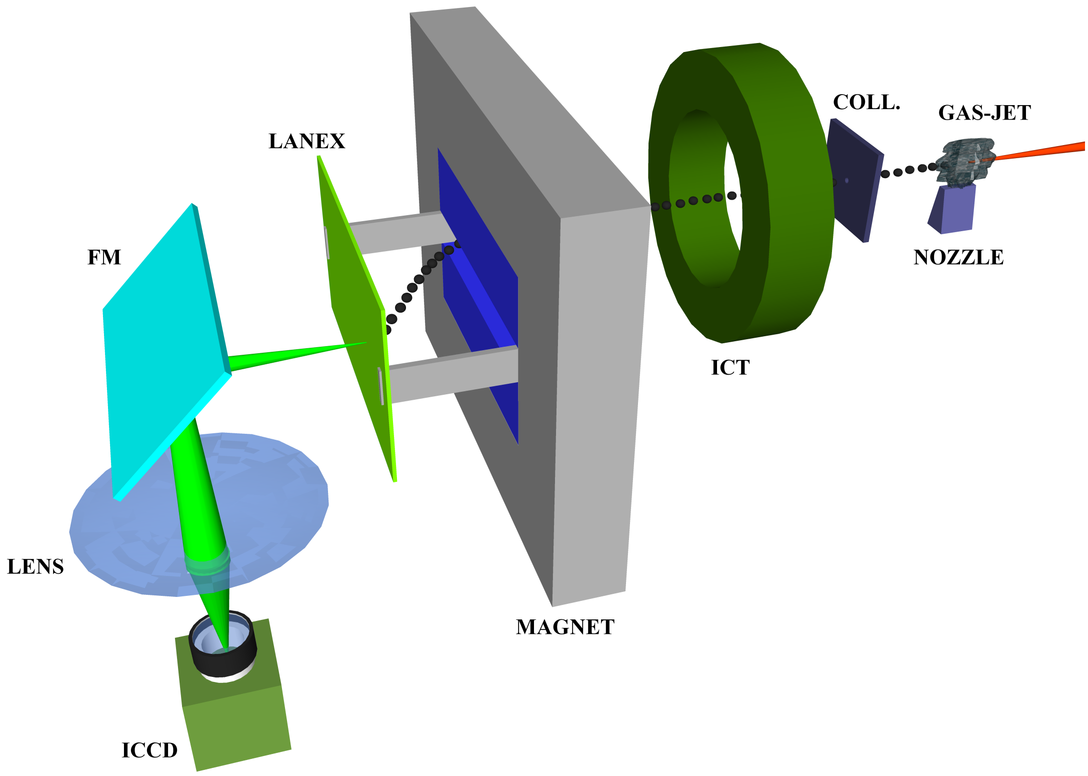

Figure 2.4: Detailed scheme of the experimental setup for electron stream generation. The generated electron beam from the supersonic gas-jet passes through the collimator, the number of particles is measured by the ICT. The magnet inside the frame is used for deflecting the electron trajectory and electron beams impact the LANEX screen. The outgoing light from the LANEX is reflected by the FM and focused by the lens and the position of the impact is recorded by the ICCD camera.

bunched beam signal. The ICT with a small inner diameter (e.g. 16 mm) must be placed close to the gas-jet. But at this position, the ICT receives low-energy electrons affecting the measurement and there is not enough space to deflect them. Thus it is better to use the ICT with larger diameter. At the beginning of the experiment it is possible that the accelerated charge is low, in this case it is useful to use the ICT with higher sensitivity. For experiment at PALS the ICT with inner diameter 55 mm and the external diameter 91 mm has been chosen.

The frame – permanent magnet system causes a magnetic field affecting the trajectory of the electron beams. Inside the frame there are two blocks of the Vacodim 745 permanent magnet (blue in figure 2.4) with a free space between them. The reason to use the iron frame is the shaping of the magnetic field space distribution and the increase of the magnetic field intensity by using a compact and cheap device. By taking into account the edge effects it is possible to calculate the magnetic field distribution and the electron trajectory and then to predict how the electrons will be deflected on the basis of their energy going towards and passing through the LANEX screen. Electrons are affected by the Lorentz force (eq. 1.6) thus deflected in one direction. For this reason it is useful to inject the electron beam into one side of the gap between the magnets in order to gain a better resolution for lower energies. More detailes are reported in the next chapter.

The LANEX screen converts the x-ray energy into green light. These screen incorporate phosphors containing metal compounds from the lanthanide series of rare-earth elements [23]. This technology provides high quality images at reduced dose. The LANEX fast screen in the experiment allows us to get a visible image of the electron impact. The screen will be used with protective coating 10 μm of cellulose acetate and 178 μm of Polyethylene terephtale, the 84 μm of Gd_2O_2S and urethane binder as a scintillator with 5 μm protective coating of cellulose acetate. To ensure the high accuracy of the experiment the LANEX screen has to be calibrated. Some low energy particles are stopped at the protective coating of the screen and the rest leave the scintillator and deposit their energy further away. Thus the conversion efficiency of the scintillator is unknown and it has to be found out experimentally, e.g. by the radiofrequency accelerator producing electron bunches at a certain values of charge and energy.

Additional optics behind the LANEX screen serves to focus produced green light from the LANEX onto the ICCD camera and to make a magnification in order to improve the spatial and, as a consequence, the energy resolution. As indicated in figure 2.3 and 2.4 the additional optics can consist of a flat mirror (FM) reflecting the green light on the lens. The lens then focuses the light onto the ICCD camera. It is also possible to use optical fibres attached to the LANEX screen and then receive the precise resolution with accuracy of the fibre size. The disadvantage when using large area of the LANEX screen is that it needs larger amount of optical fibres and greater device (or more devices) to light intensity detection.

The ICCD camera is a high sensitivity device capable of single photon detection. It is the charge-coupled device (CCD) which is optically connected to an image intensifier mounted in front of CCD. The image intensifier includes three functional elements: a photocathode, a micro-channel plate (MCP) and a phosphor screen. These three elements are mounted one close behind the other in the mentioned sequence. The reason of the image intensifier is that once a photon reaches the photocathode, the photoelectron is generated. The photoelectrons are accelerated toward the MCP by a controlled electrical voltage and they are multiplied inside the MCP and further accelerated to the phosphor screen. The phosphor screen convert electrons back to the visible light which is registered by the CCD. If the voltage between photocathode and MCP is reversed, electrons are repulsed from MCP and no signal will be registered by CCD. This voltage reversion process is called gating and it helps to select incoming light intensity information between specific time intervals. In the experiment the ICCD camera will have the 1024×256 array and true optical gating as short as 1.2 ns.

2.3 Quasi-monoenergetic proton streams

The experimental setup for the generation of the monoenergetic proton/ion beams is simpler than for electron beams when using a time-of-flight (TOF) measuring method. The TOF method will be discussed further in chapter 3.2 together with the Ion Collector (IC) device used for TOF measurements. The IC analysis can be accompanied by the Thomson Parabola analyzer (TP) used for ion energy estimation and the Ion Energy Analyser (IEA) for recognizing different charge states. It is expected to accelerate ions in two different regimes: TNSA and SLPA. In both methods the laser beam is focused onto a solid target. These two accelerating methods differ from each other in the thickness of the target, for TNSA method the thickness of the target ranges between 0.1 and 100 μm, whereas for SLPA method the target thickness must be greater than 1 mm.

2.3.1 TNSA experimental setup

The experimental setup of the TNSA method can be sketched as in figure 2.5. The laser beam coming from the laser system is reflected onto the OAPM and focused onto the target. The target can consist of single layer only, or double layer. The optimum target thickness and the target structure have to be found experimentally because the proton beam energy and total charge essentially depends on these parameters. Plasma is generated along the direction normal to the target by the mechanism described in chapter 1.2.2. The quasi-monoenergetic proton stream originates from the plasma together with the X-UV radiation. The radiation approaches to the IC earlier than protons. The current of the proton stream is collected at the IC and registered by a fast storage oscilloscope.

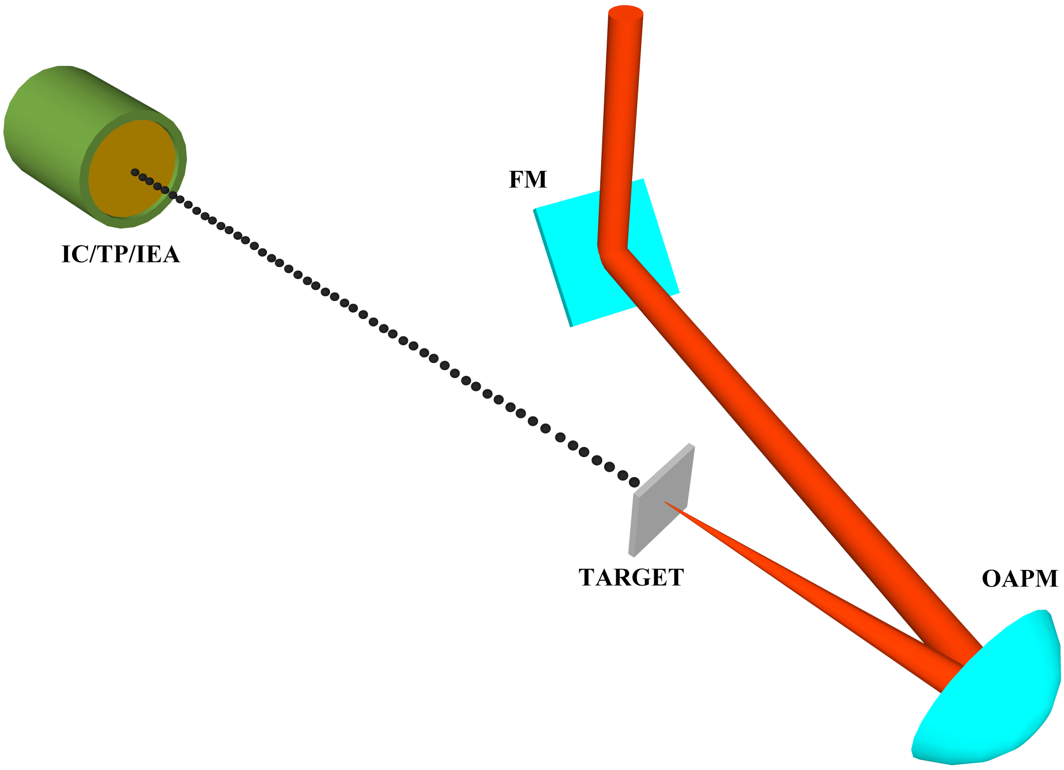

Figure 2.5: Scheme of the TNSA method. The laser beam is focused by the OAPM onto the target surface. The accelerated ion stream is generated at the rear side of the target and approaches to the IC (and/or TP, IEA) where the current of the beam and the TOF is measured.

There are two possible configurations of the target in TNSA mechanism. The first one uses a single layer target with the impurities mainly on the rear side. The target is usually made of a good absorber of hydrogen (e.g. titanium, palladium). After collision with the laser pulse, the stream of ions is generated at the target rear side.

The second one uses a double layer target. In order to raise the laser energy conversion when using the double layer target the front layer has to be metal with high free electron density (e.g. gold, tantalum) which provide the large amount of electrons accelerated through the rear layer. The rear layer is usually made of hydrogen-rich compounds or polymers. Therefore high proton concentrations are generated from the second layer. The thickness of the rear layer is usually about tenths of micrometers and its width can be optimized by performing ablation on the target rear side by means of the femtosecond laser itself, in order to improve the monoenergeticity of the beam [18].

It is also possible to use the so-called mass limited targets (MLT), i.e. small targets with all dimensions less or comparable to the laser spot diameter in order to minimize the effect of an inhomogeneous electric field at the target edges. Interaction of ultrashort laser pulses with MLT can result in unique phenomena due to their geometry and small size [24].

2.3.2 SLPA experimental setup

The experimental setup of the SLPA method can be as the one reported on the scheme in the figure 2.6. The laser beam is focused by the OAPM onto the thick target (much thicker than the TNSA method). The preplasma is generated by the foot of the main laser pulse and then the main pulse generates ion stream and accelerate it in backward direction to the laser beam propagation by the mechanism described earlier in chapter 1.2.2. The generated ion beam gives a limitation for location of the measurements due to its low angular divergence, i.e. the IC must be placed as close as possible to the target normal direction.

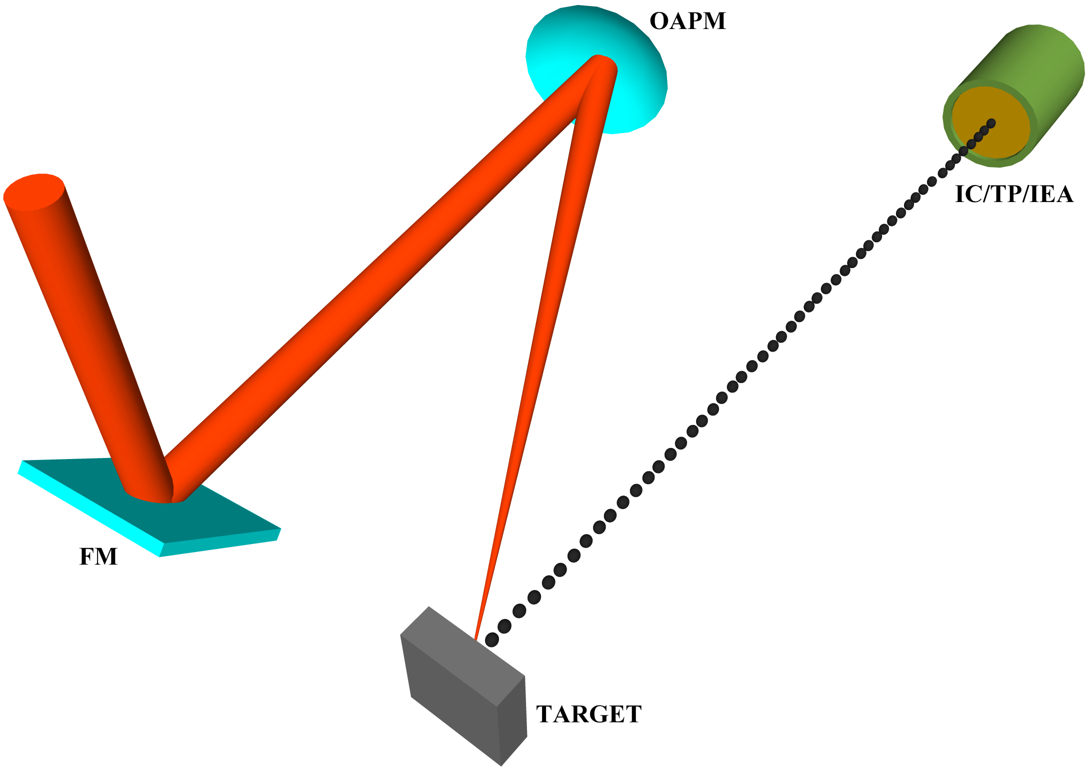

Figure 2.6: Scheme of the SLPA method. The laser beam is focused by the OAPM onto the thick target surface. The ion stream is generated and accelerated in backward direction to the laser beam propagation and the characteristics of the stream are detected by the IC and/or TP, IEA.

Similarly to the case of TNSA, parameters of forward-emitted proton beams produced by SLPA significantly depend on the thickness and structure of the target used. In particular, using double-layer targets makes it possible to produce higher proton energies and proton currents than in the case of single-layer targets [8].

TNSA method enables to work at repetition rate of the laser, because it is possible to construct a roto-translating target (i.e. the target makes rotation and translation motion between two laser shots).

2.3.3 Ion energy analyser

The ion energy analyser (IEA) is a device aimed to determine ion energy distributions and abundances of ion species in the plasma [25]. The main part of the IEA is a deflection system consisting of two coaxial metallic cylinders (R_1 inner radius and R_2 outer radius) charged at a proper potential (V_1 and V_2). The schematic draw of the IEA is reported in figure 2.7.

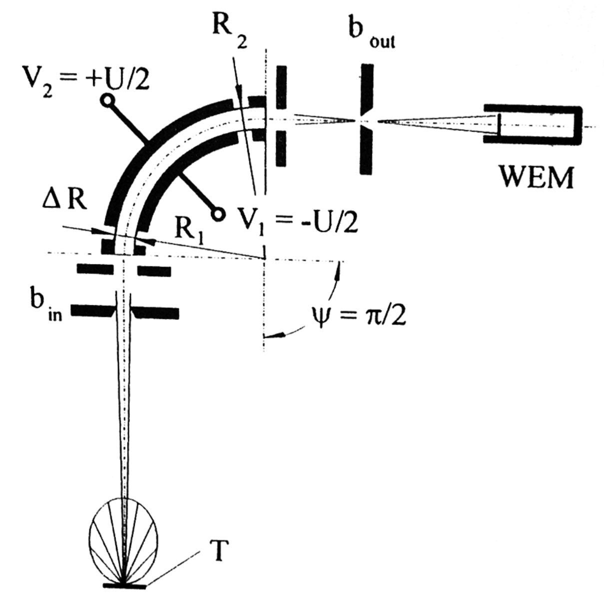

Figure 2.7: Scheme of the IEA. Plasma is produced at the target T heading to the deflection system of the IEA and further to the detector WEM (windowless electron multiplier). The input and output slits b_{in} and b_{out} collimate the ion beam entering and leaving the IEA [25].

The ion trajectory is deflected by a radial electric field inside the deflection system. When the equilibrium between the centripetal force acting on an ion with charge state z and the force affecting the ion in the radial electric field of the deflection system occurs, the energy-to-charge state ratio is:

$$\frac{E}{z} = \frac{e\,(V_2 - V_1)}{2ln\,(R_2/R_1)} \tag{2.5}$$

where e is the elementary charge, the inner radius is $R_1 = 10.25$ cm and the outer radius is $R_2 = 10.5$ cm. If the cylinders are charged at potential $V_2 = -V_1 = 3$ kV and we want to measure the carbon ion C^{5+}, its energy is $E = 622$ keV. Considering:

$$E = \frac{1}{2}Mv^2 \tag{2.6}$$

where M is the mass of the ion and v is the velocity given by the ratio between the distance L of the detector and the time of flight (TOF), i.e. the time needed for ion to reach the distance L. From equations 2.5 and 2.6 the TOF is

$$\tau = L\sqrt{\frac{M}{z}\frac{ln\,(R_2/R_1)}{e\,(V_2 - V_1)}} \tag{2.7}$$

For the same values of R_1, R_2, V_2 and the distance $L = 2$ m the time of flight of the C^{5+} will be $\tau = 6.3 \times 10^{-7}$ s. As can be seen from equation 2.7 that only ions with certain charge-to-mass ratio can pass through the IEA and reach the detector. The detector WEM registers the voltage caused by the impact of the ions depending on their time of flight. For known IEA parameters and TOF the charge-to-mass ratio is determined from equation 2.7.

The main disadvantage of the IEA is the requirement of a large number of laser shots in order to obtain the ion energy distribution [25]. Moreover, the maximum voltage which is possible to bring on the coaxial metallic cylinders gives the limitation to detection in the maximum proton energy at a value of 0.6 MeV.

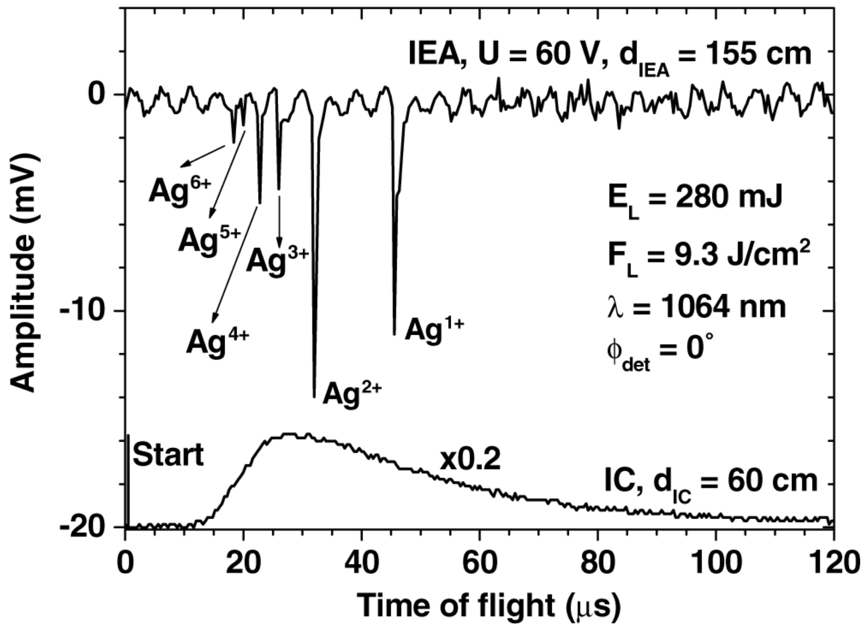

Figure 2.8: Typical IEA spectrum (upper signal) [26].

2.3.4 Thomson parabola

The Thompson parabola (TP) is a mass spectrograph. Charged particles propagate through the TP and are deflected by static electric and magnetic fields parallel to each other and perpendicular to the motion of the charge particle stream. The stream is registered at the imaging plane.

Ions are influenced by the electric and magnetic field and their trajectory is a consequence of the laws of motion, i.e. when charged particles enter the direction perpendicular to the parallel fields, the particles will draw the parabola on the imaging plane. The equation of the drawn parabola is

$$y^2 = \frac{z}{M}\frac{eB^2LD}{E}x \tag{2.8}$$

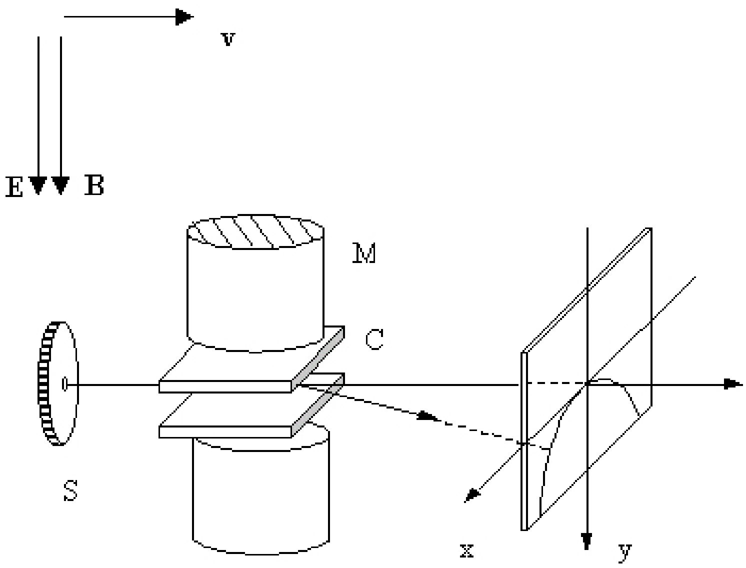

Figure 2.9: Thomson parabola analyzer. Particle stream propagates through the parallel **E** and **B** field initiated by permanent magnet M (or electromagnet) and capacitor C and ions are separated due to their charge-to-mass ratio and impact the imaging plane.

where B and E are magnetic and electric parallel fields, L is the length of the capacitor and D is distance from the end of the capacitor to the registration plane. For C^{5+} ion, capacitor length $L = 10$ cm, distance from capacitor to imaging plane $D = 20$ cm, magnetic field $B = 1$ mT, voltage on capacitor $V = 1$ kV, distance between capacitor plates $b = 2$ cm, thus electric field is 20 Vm^{-1}, coordinate $x = 5$ cm the y coordinate according to equation 2.8 is 4.48 cm.

The ion energy ϵ can be determined e.g. from the x coordinates which is equal to

$$x = DL\frac{zeE}{2\epsilon} \tag{2.9}$$

The energy from equation 2.9, taking into account the above reported values, is $\epsilon = 20$ eV.

Both x and y coordinates depend on the ion energy. The point of origin of the plane is given by the impact of neutral particles and X-UV radiation from plasma. It is seen from equation 2.8 that an ion stream with a certain value of the charge-to-mass ratio will draw a different parabola than for streams with different ratios. From equation 2.9 it is seen that more energetic particles are closer to the apex of the parabola. Recording system of TP can have two different types of detectors, track detectors or image converter with an MCP of high diameter as an amplifier [25]. The widths of the parabolas are influenced by the quantity and charge state of the ions, the time of flight and the geometry of the measurements. It can also be seen from the experiments that ions of certain charge-to-mass ratio with lower energy are more affected by the space charge than ions with higher energy, thus the parabola is wider for ions with lower energy.

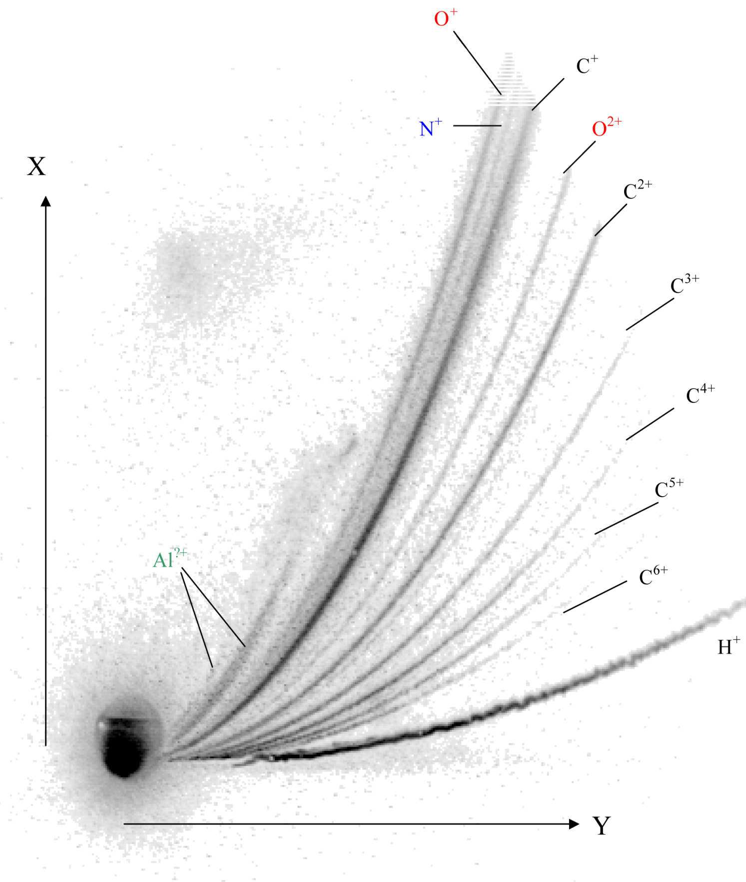

Figure 2.10: Typical TP spectrum. The graphite target was used with the oxygen, hydrogen and nitrogen impurities.

Chapter 3

Selection and preliminary tests of proper diagnostics methods

3.1 Magnetic electron spectrometer

When a fast particle beam is produced, the first and most important measurement is the energy distribution estimation. In order to estimate the relativistic electron stream distribution we designed a proper magnetic spectrometer. The magnetic spectrometer is composed of a permanent magnet or a coil making magnetic field favourable for deflecting the electron streams. The deflection depends on the particle velocity (energy). The faster are the particles the weaker is the deflection.

The magnetic spectrometer will be used in the experiment for its advantages over electrostatic spectrometers. The advantages generally are: the simplicity of manufacture; the absence of edge effects if the beam goes through the constant magnetic field region; the possibility of installing aperture diaphragms in the electron beam trajectory within the focusing magnetic field, which decreases the noise and increases the contrast; the possibility of implementing the multichannel mode of electron detection; the independence of the aperture ratio and resolution of the electron energy [27].

Considering the parameters of the laser system and results of [14, 16] it is expected (with 40 fs pulse length, 800 nm wavelength and about 1 J of the laser pulse energy) to produce stable electron beams (in the bubble regime) within the range of 100–200 MeV with a beam charge of hundreds of pC.

For our experiment two blocks of Vacodim 745 permanent magnets are set in an iron frame in order to produce a magnetic field as homogenous as possible. The deflection should be as on figure 3.1.

As it can be seen from figure 3.1 the motion of the stream is not exactly on the magnet axis but it is still in a region of maximum magnetic field intensity. The reason is to raise the deflection and the sensitivity for slower particles.

The electrons are bent on the right direction in figure 3.2 where the field inside the magnet is almost homogenous and calculations for the calibration should be easier. By using TOSCA-VECTOR FIELD Simulations [28] the final energy distribution on the LANEX screen can be calculated as shown in figure 3.3.

The simulations of the input (at the entrance of the magnetic spectrometer) electron beam assume Gaussian spatial and energy distribution peaked at 400 MeV, with an energy spread of 35% at FWHM and 30 mrad angular divergence of the beam. With this input it is possible to obtain the output on the LANEX at different distances.

It is possible to increase the energy resolution for higher beam energies by moving

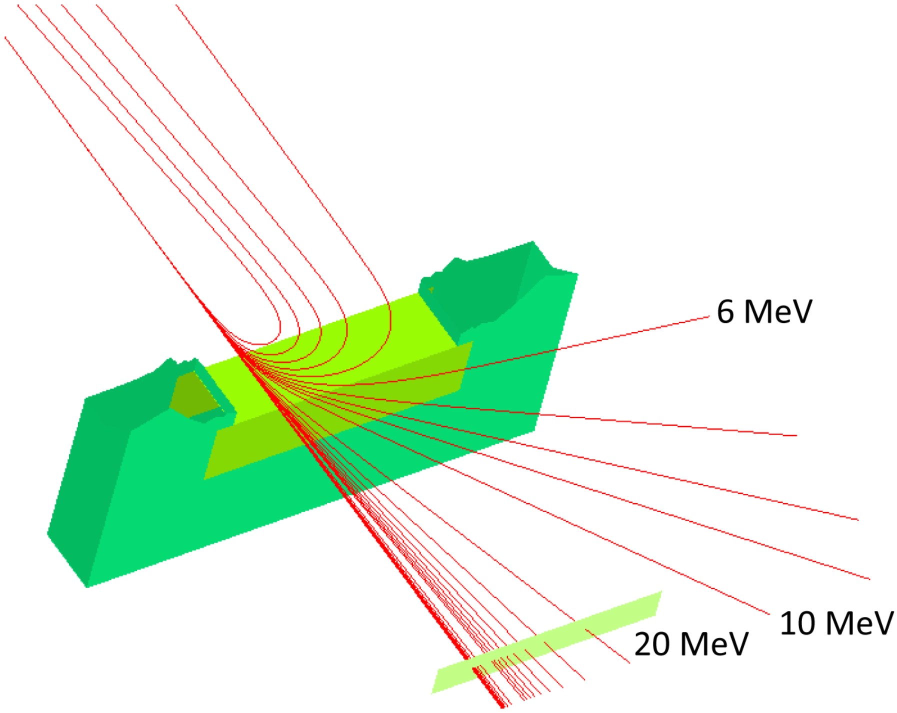

Figure 3.1: Scheme of the electron deflection in the space between two permanent magnets. The deflection depends on the particle velocity. Faster particles reach the LANEX phosphorus screen and their energy can be measured.

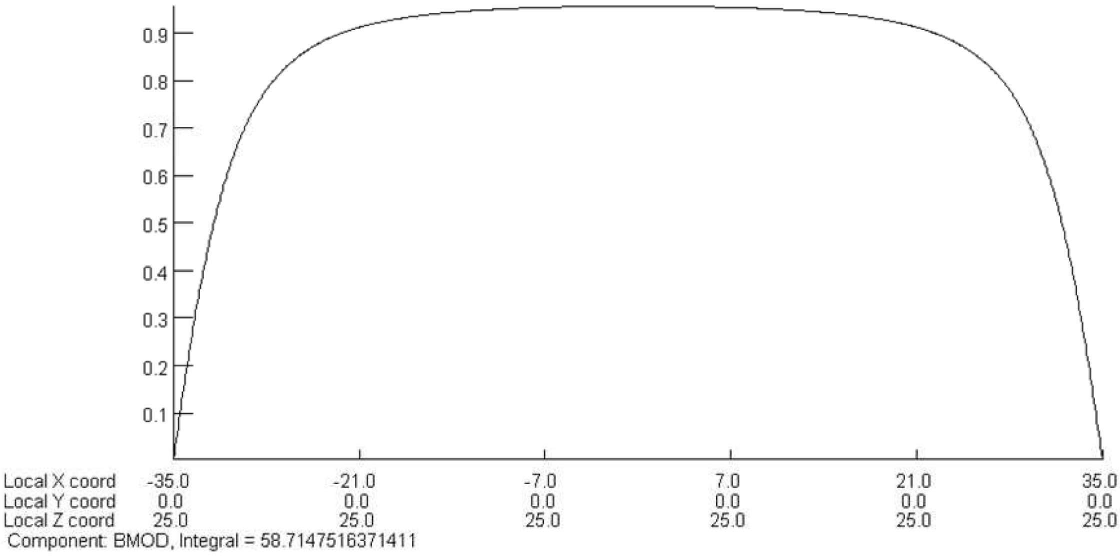

Figure 3.2: Magnetic field inside the permanent magnets and its frame perpendicular to the particle motion. X coordinate corresponds to the width of the magnet with the origin in the centre of the magnet, Y corresponds to the height of the magnet and Z corresponds to the beam propagation direction also with the origin in the centre of the magnet.

the LANEX screen far away from the magnet. The cost of rising resolution is losing the sensitivity of the screen for lower energy streams.

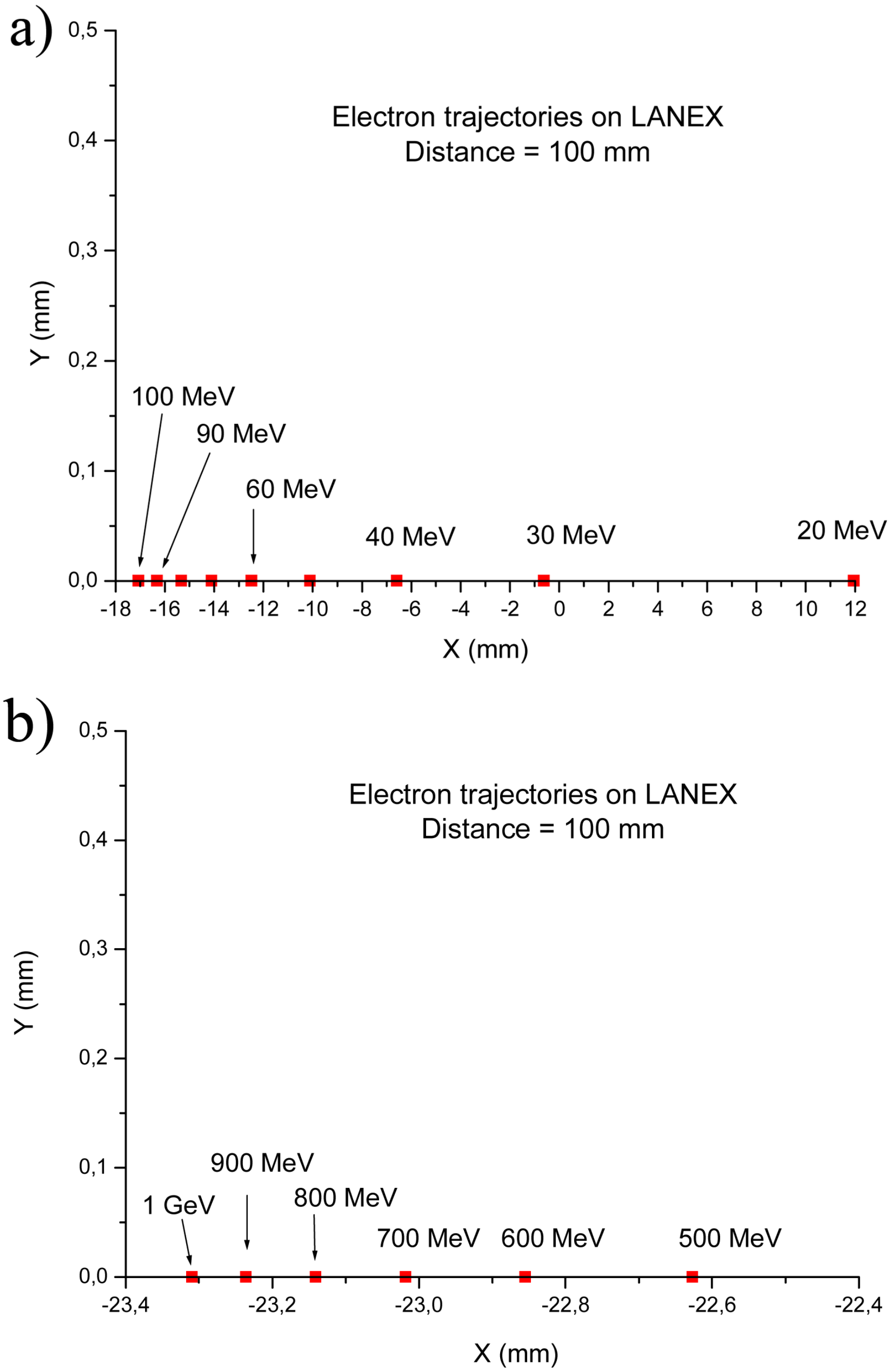

Figure 3.3: Energy distribution on the LANEX screen placed 10 cm behind the magnet. a) shows a resolution for lower electron energies, the energy range 90–100 MeV corresponds to 750 μm on the LANEX and 30 pixels on the ICCD planned to be used, which leads to 0.3% of energy resolution whereas b) shows the energy distribution for higher energies, where energy range 0.9–1 GeV corresponds to 75 μm on the LANEX and 3 pixels on the same ICCD leading to 3% of energy resolution.

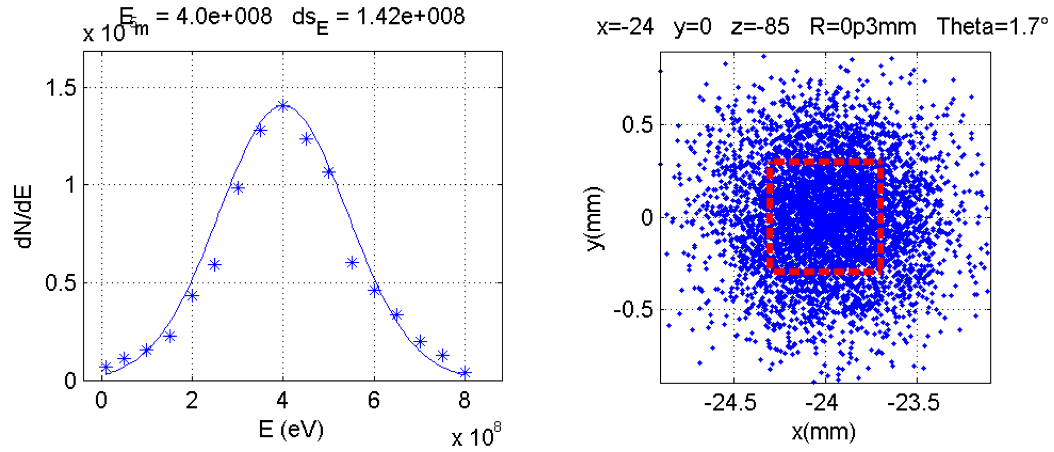

Figure 3.4: TOSCA-VECTOR FIELD Simulations of the Gaussian spatial profile of the electron beam and its divergence on x and y axis (the z axis corresponds to the motion direction of the beam) at the entrance of the magnetic spectrometer.

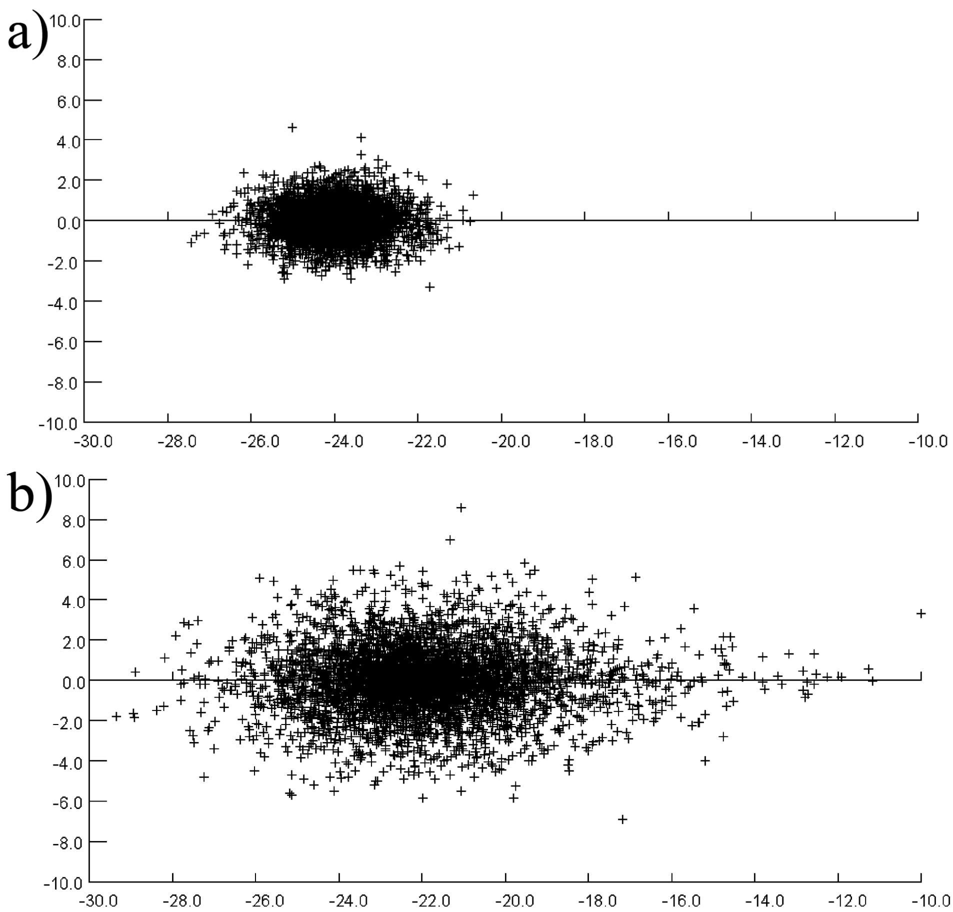

Figure 3.5: Beam spatial distribution on the LANEX screen depending on the distance from the magnet, a) LANEX position is 1 mm behind the magnet and b) 100 mm behind the magnet.

3.2 IC-TOF measurements by proper filtering

It is possible to estimate the maximum proton energy gain as [29, 30]:

$$E_{max} = 2T_{hot}\left[ln\left(t_p + \sqrt{t_p^2 + 1}\right)\right]^2 \tag{3.1}$$

where T_{hot} is the plasma temperature and t_p is

$$t_p = \frac{\omega_{pi} t_{acc}}{\sqrt{2e}}; t_{acc} \sim 1.3\tau_{laser} \tag{3.2}$$

where ω_{pi} is plasma ion frequency, τ_{laser} is the laser pulse length, τ_{acc} is the acceleration time. Increasing the pulse length would lead to the generation of higher proton energies. But when we want to generate fast electron beams, it is better to have shorter pulse lengths in order to increase the intensity producing a greater ponderomotive force strongly responsible for acceleration. According to equation 3.1 it will be possible to produce maximum proton energy of about 1 MeV with the Ti:Sapphire laser system at PALS.

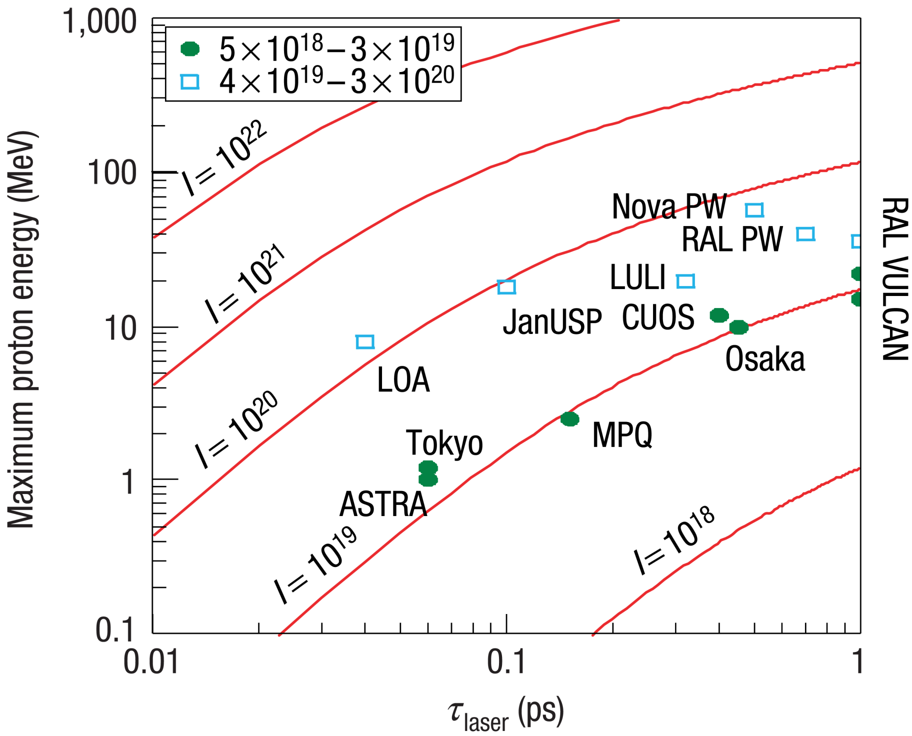

Figure 3.6: Scaling for maximum proton energy gain strongly depends on the pulse length (and the laser intensity) [31].

The ion collector (IC) is a plane collector or a Faraday cup aimed to measure the ion component of a plasma produced from the laser-target interactions. The IC permits ion and electron separation usually done by means of a static electric field between the grounded entrance grid and the negatively biased collector. The ion current is collected by a biased collector and it is measured by means of a fast storage oscilloscope. If ions reach the collector it causes the secondary electron-ion emission that may be suppressed by using a metal grid. The schematic draw of the IC is on figure 3.7.

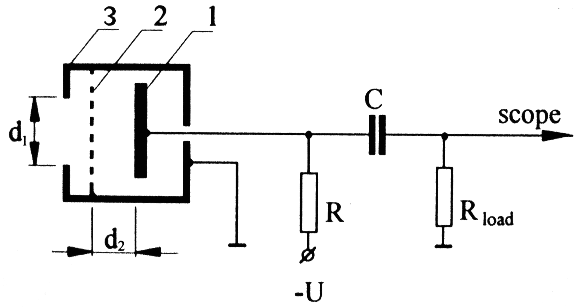

Figure 3.7: Scheme of the IC. 1 - collector, 2 - entrance grid, 3 - grounded housing, d_1 - diameter of the entrance aperture, d_2 - spacing for electron and ion components separation, U - bias potential, R_{load} - load resistance [25].

Neglecting the secondary ion-electron emission and shielding grid the current density is:

$$I_i = en_e v = ev \sum_{j=0}^{Z_{max}} z_j n_{i,j} \tag{3.3}$$

where e is elementary charge, n_e is an electron density and v is the plasma velocity, j is the number of ion species, $n_{i,j}$ is the density of the j^{th} ion specie and z_j is the charge state of the j^{th} ion specie. Using the biased collector, the space charge layer is formed and shields the collector from the plasma. The threshold ion density for this effect is approximately given by

$$n_{i,z}\left[cm^{-3}\right] \leq 2.5 \times 10^8 \frac{E\,[keV]}{z \cdot d_2\,[cm]} \tag{3.4}$$

where E is the kinetic energy of ions with the charge state z, d_2 is the distance between grid and collector, $n_{i,z}$ is the density of ions with the charge state z. It can be seen from equation 3.4 that ions with the lower energy and charge state are more severely limited by the space charge. For a grid-collector distance of 2 cm, ion energy 1 keV for the charge state 5+, the threshold limitation for the ion density is 2.5×10^6 cm^{-3}.

The output current I_c in the collector circuit is a combination of ion current I_i and secondary electron current I_e:

$$I_c = I_i + I_e = e\epsilon vS \left\{ \sum_{j=0}^{Z_{max}} \left[z_j(t) + \gamma_j(t)\right] n_{i,j}(t) \right\} \tag{3.5}$$

where ϵ is the transparency of the entrance grid, S is the area of the collector, γ_j is the secondary ion-electron emission coefficient, z_j is the charge state, $n_{i,j}$ is the density of the j^{th} ion species where $j = 0$ corresponds to the neutral particles. Taking into account that $ni = \sum n_{i,j}$ in equation 3.5 we can write

$$I_c(t) = \epsilon evS\overline{z}(t)\, n_i(t) \left[1 + \frac{\overline{\gamma}(t)}{\overline{z}(t)}\right] = \epsilon \left[1 + \frac{\overline{\gamma}(t)}{\overline{z}(t)}\right] I_{coll}(t) \tag{3.6}$$

where $\overline{\gamma} = \sum_j \gamma_j n_{i,j} / \sum_j n_{i,j}$ is the average secondary ion-electron emission coefficient, $\overline{z} = \sum_j z_j n_{i,j} / \sum_j n_{i,j}$ is the average charge state of ions and I_{coll} is the ion current in the entrance grid for a given moment t. Then form equation 3.6 the ion current on the entrance grid is:

$$I_{coll}(t) = \frac{U_C(t)}{\epsilon R_{load}\left[1 + \frac{\overline{\gamma}(t)}{\overline{z}(t)}\right]} \tag{3.7}$$

where $U_c(t)$ is the voltage amplitude of the collector signal and R_{load} is the load resistance. From equation 3.7 it is also possible to obtain the velocity and energy distribution.

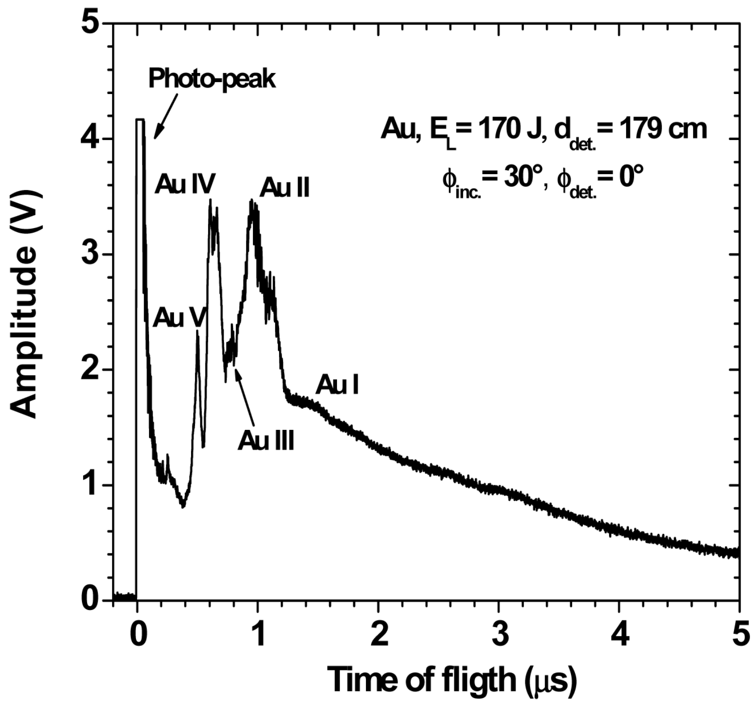

Figure 3.8: Typical IC spectrum [32].

When the laser hits the target, plasma and accelerated ions are generated together with XUV radiation from the plasma. The radiation spreads through the chamber and reaches the IC as first causing a secondary electron emission from the grid and, as a consequence, a voltage amplitude (called photo-peak) at the output signal, as it can be seen from figure 3.8. The photo-peak serves as a trigger for the time measurements.

An expected advantage of IC in experiments with Ti:Sapphire laser system is the XUV radiation generated in plasma will last tens of femtosecond according to the laser pulse duration. The photo-peak should be very narrow and it should be possible to measure directly the ion current for each laser shot.

Widely more than one IC is used in the experiment where at least one of the IC is shielded by a filter of thickness of few micrometres. It is also possible to divide the IC into four quadrants and to cover each quadrant with the foil of the different thickness and/or geometry.

This technique permits to have simultaneously information from the whole plasma emission (XUV, fast and slow ions) and only from different ion energy ranges (depending on the filter thickness).

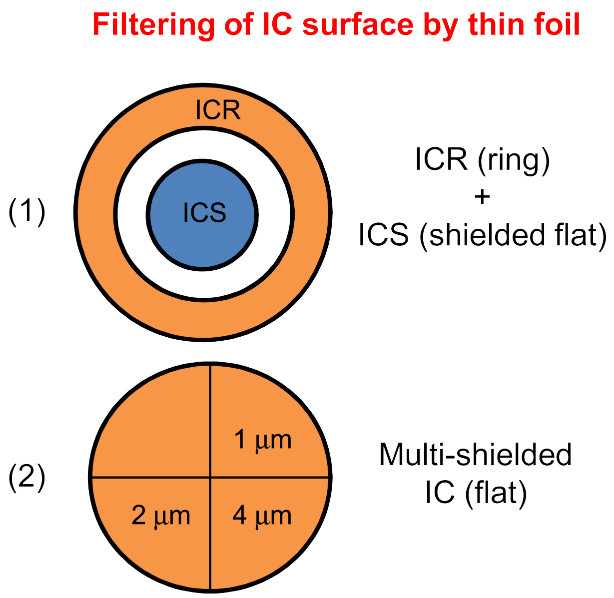

Figure 3.9: Scheme of the IC shielded (1) with a shield in one piece and (2) with divided area covered by several.

The XUV radiation can be cut by using Au and Ta filters of thickness 1–5 μm. The figures below report the transmission of the XUV radiation in different metallic filters [33].

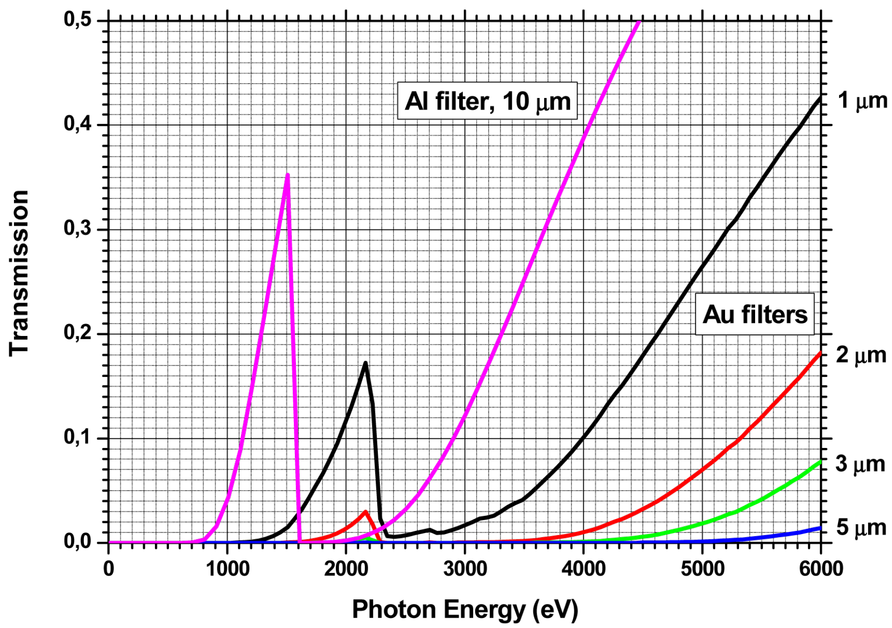

Figure 3.10: Transmission of XUV radiation depending on photon energy for Au filter of thickness 1, 2, 3 and 5 μm and Al filter of thickness 10 μm. The 10 μm Al filter cuts the photon energy less than 800 eV and the 1 μm Au filter cuts the photon energy less than 1.3 keV.

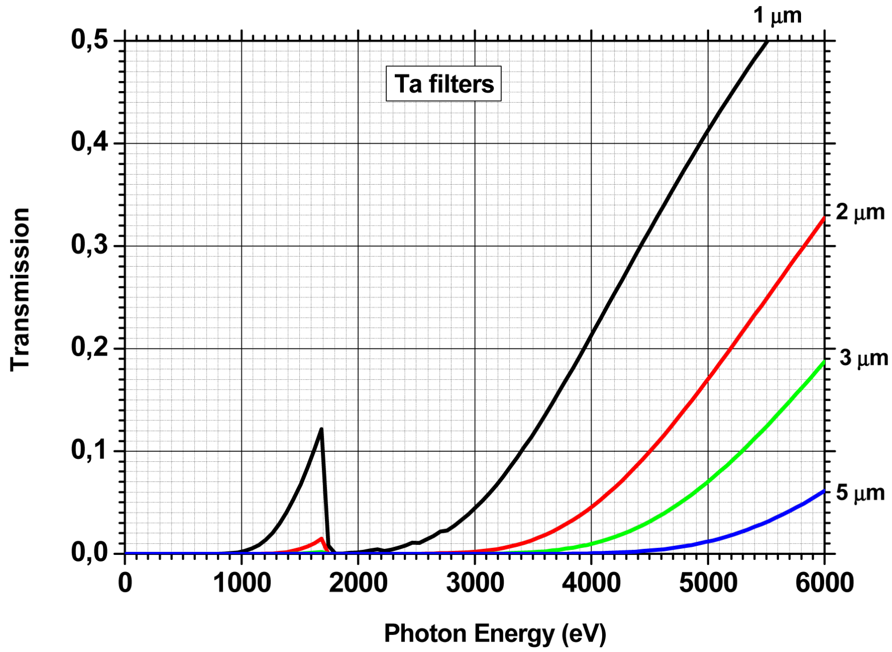

Figure 3.11: Transmission of XUV radiation depending on photon energy for Ta filter of thickness 1, 2, 3 and 5 μm. The 1 μm Ta filter cuts the photon energy less than 1 keV.

The filtering technique causes the spread in energy distributions of the ions due to the interactions with the filter atoms. The energy loss of the ions depends on their own energy. This problem can be reduced if a light element filter is used (e.g. Al filter), but on the other hand, the XUV transmission increases (as reported on figure 3.10). If the filter is placed few millimetres from the IC the change in TOF is negligible because the target-collector distance is usually long, thus the energy spread is negligible. The filter does not cut only the XUV radiation, it also cuts low energy ions and disable their further detection. The cut-off energy can be predicted by SRIM simulations. The table below reports the cut-off energies of the elements in the filter.

SRIM is a group of programs which calculate the stopping and range of ions (10 eV – 2 GeV /amu) into matter using a quantum mechanical treatment of ion-atom collisions. During collisions, the ion and atom have a screened Coulomb collision, including exchange and correlation interactions between the overlapping electron shells. The ion also has long range interactions with target atoms creating electron excitations and plasmons (plasmon is a quantum of a collective oscillation of charges on the surface of a solid induced by a time-varying electric field) within the target. These are described by including a description of the target collective electronic structure and interatomic bond structure when the calculation is setup. The charge-state of the ion within the target is described using the concept of effective charge, which includes a velocity dependent charge state and long range screening due to the collective electron sea of the target [34].

If the ion is not stopped in the filter, it is slowed and its energy decreases, whereas its energy spread increases. The ion energy spread is given as:

$$\sigma - \frac{E_M - E_m}{E_p} \tag{3.8}$$

and it is mainly given at FWHM which means the E_p is a peak of energy and $E_M - E_m$ is an energy range at half of the peak.

Ion Beam	Filter Thickness (μm)	Cut-off Energy of Au filter (MeV)	Cut-off Energy of Ta filter (MeV)	Cut-off Energy of Al filter (MeV)
H	1	0.275	0.25	0.12
H	2	0.5	0.45	0.25
H	3	0.65	0.6	0.325
H	5	1	0.9	0.5
C	1	2	1.7	0.65
C	2	5.5	4.5	1.8
C	3	9	8	3.25
C	5	15	14	6
Ti	1	4.5	4	1.4
Ti	2	13	11	3.5
Ti	3	25	22.5	6.5
Ti	5	60	50	15

Table 3.1: The cut-off energy of H, C and Ti elements in Au, Ta and Al filters in the thickness range 1–5 μm predicted by SRIM simulations.

When the ion has an initial energy E_i and passes through the filter losing an energy δE, its final energy will be:

$$E_M = E_i - \delta E \tag{3.9}$$

The energy lost caused by the ionization in the filter can be calculated using TRIM simulations.

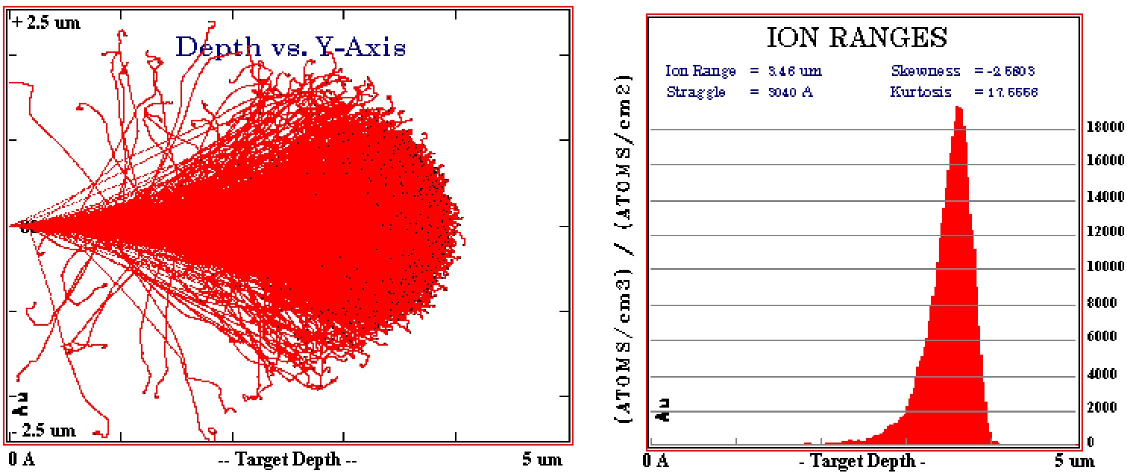

Figure 3.12: Example of longitudinal distribution and the ion ranges inside the Au target by using TRIM simulation for C element with energy of 10 MeV.

TRIM (the Transport of Ions in Matter) is a Monte-Carlo calculation which follows the ion into the target, making detailed calculations of the energy transferred to every target atom collision. TRIM will accept complex targets made of compound materials with up to eight layers, each of different materials. It will calculate both the final 3D distribution of the ions and also all kinetic phenomena associated with the ion's energy loss: target damage, sputtering, ionization, and phonon production. All atom cascades in the target are followed in detail. The program is made so it can be interrupted at any time, and then resumed later. The calculation is made very efficient by the use of statistical algorithms which allow the ion to make jumps between calculated collisions and then averaging the collision results over the intervening gap [34].

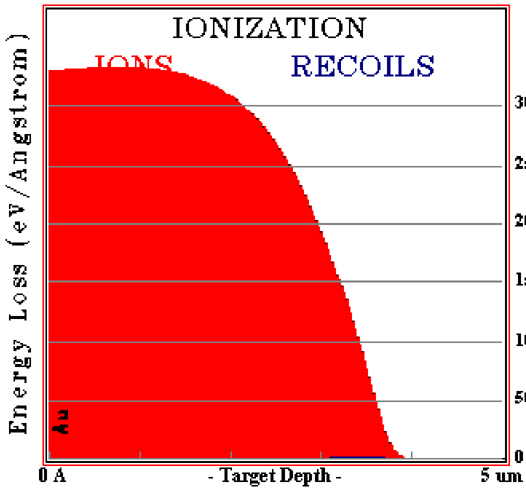

Figure 3.13: Example of the ionization inside the Au target by using TRIM simulation for C with energy of 10 MeV.

As it is shown in the figure 3.13 the energy loss is the red area. The recoils (blue area) are negligible in comparison with the energy loss caused by the ionization. For initial energy peak and energy spread we can use TRIM calculation to obtain the peak of energy and energy spread behind the filter. The two following tables give examples of this technique.

Ion Beam	Ion Range (μm)	Initial Energy E_i (MeV)	Initial FWHM σ_i (%)	Final Energy E_f (MeV)	Final FWHM σ_f (%)	Energy Shift $\delta E/E_i$ (%)	Peak TOF (ns) at 2 m
H	6.25	1	40	0.77	58.4	23	144
H	195.14	10	40	9.94	40.4	0.6	45.5
H	2860.00	50	40	49.98	40.0	0.04	20
C	2.23	5	40	0.46	169.6	90.8	223
C	20.99	50	40	46.25	45.0	7.5	70
C	236.52	250	40	248.72	40.3	0.5	31
Ti	2.79	18	40	3.88	67.3	78.4	235
Ti	12.86	180	40	147.33	50.2	18.2	74
Ti	78.73	900	40	883.39	41.1	1.8	33.2

Table 3.2: Interaction parameters calculated by using TRIM simulation for a given ion beam in 2 μm Ta filter.

TRIM simulation also showed that for lower initial ion energies there are higher energy losses. As a consequence, it can be seen from table 3.2 and 3.3, the higher is the energy loss (higher energy shift) the higher is the final energy spread at FWHM.

Ion Beam	Ion Range (μm)	Initial Energy E_i (MeV)	Initial FWHM σ_i (%)	Final Energy E_f (MeV)	Final FWHM σ_f (%)	Energy Shift $\delta E/E_i$ (%)	Peak TOF (ns) at 2 m
H	14.38	1	40	0.9	47	10	144
H	622.71	10	40	9.98	40.1	0.2	45.5
H	10,750	50	40	49.99	40	0.01	20
C	4.49	5	40	2.39	82.1	52.2	223
C	55.28	50	40	48.72	41.8	2.6	70
C	769.38	250	40	249.64	40.1	0.1	31
Ti	5.76	18	40	9.31	61.1	48.3	235
Ti	32.36	180	40	168.64	43.5	6.3	74
Ti	246.74	900	40	895.2	40.4	0.5	33.2

Table 3.3: Interaction parameters calculated by using TRIM simulation for a given ion beam in 2 μm Al filter.

However we calculated that the difference in TOF method for shielded and unshielded IC is negligible due to the distance between the shielding foil and the IC in comparison with the distance between the shielding and the target. If the target-IC distance is 2 m and the shielding-IC distance is 1 mm, ions will fly practically 2 m with the velocity gained during the acceleration and 1 mm slower according to their energy loss. If only high energy ions are in the centre of our interests, the TOF method has a very high accuracy.

3.3 Preliminary tests in TOF configuration

At PALS were performed various preliminary tests aimed to check the feasibility of the shielded IC measurements prefiously described. Experiments were made by using the iodine laser system reaching 1 kJ of pulse energy at the fundamental wavelength of 1315 nm (noted as 1ω). The pulse length is about 350 ps and the laser intensity reaches 3 TW. It is possible to convert the laser beam into the third (438 nm) harmonic frequency. Several IC were set at different angles. The most important were two flat detectors placed at the same distance from the target, one was shielded (ICS) and the other was not (ICD). An IEA was used in order to have information about the ion charge state distribution. The experiment was made inside the vacuum chamber at a pressure condition of 10–5 Pa where the collisions between plasma ions and the remaining particles are negligible. The SLPA method was used for accelerating ions.

First the experiments were made under the conditions of 3ω laser frequency and laser energy of about 30 J. The target was a gold sheet.

For known TOF and target-detector distance d the velocity of the ion and its energy can be calculated

$$v = \frac{d}{TOF} \Rightarrow E = \frac{1}{2}mv^2 \tag{3.10}$$

for non-relativistic cases, where m is the particle mass.

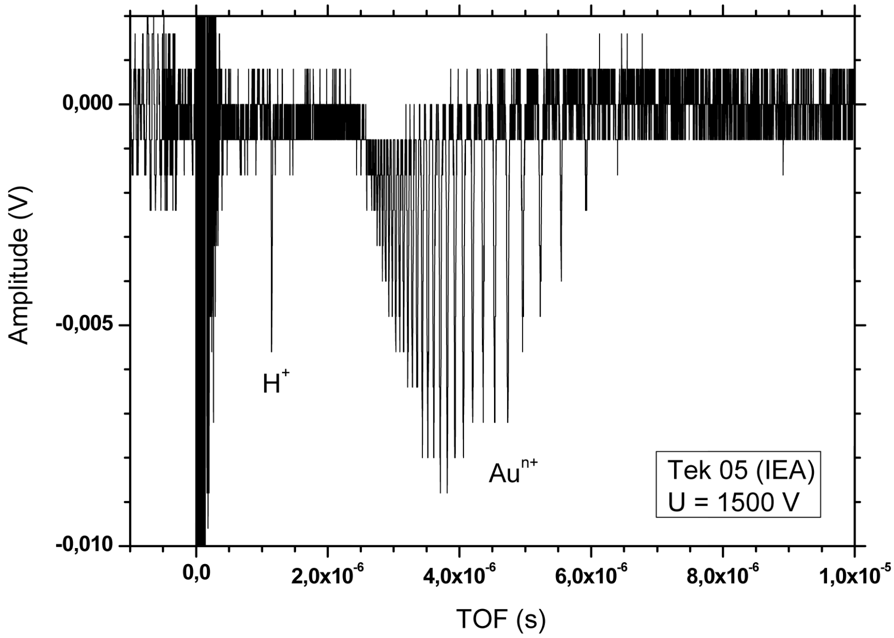

Figure 3.14: Result in TOF configuration using the IEA. There are visible peaks of Au^{n+} and also the hydrogen impurities.

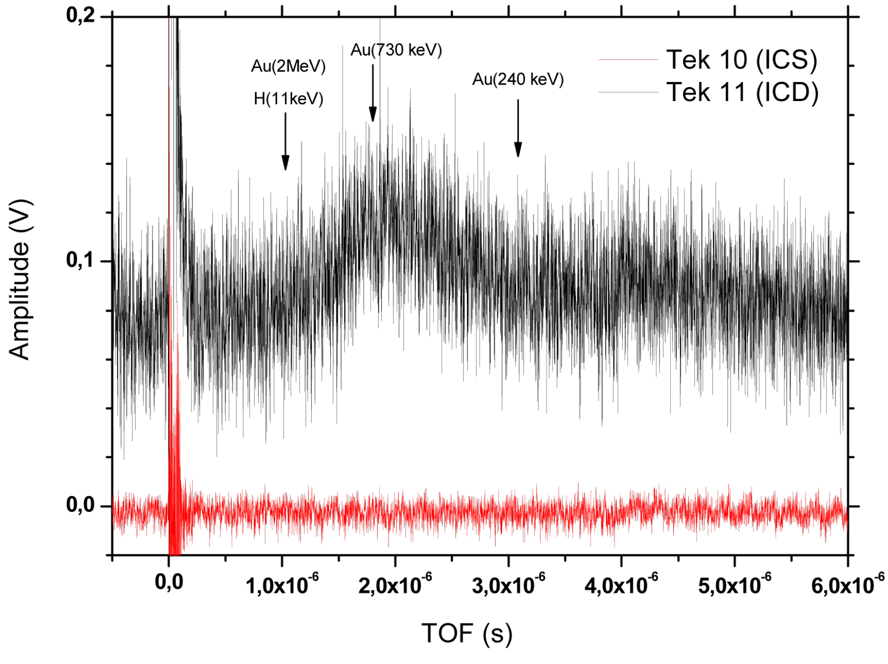

Figure 3.15: Result in TOF configuration using a shielded ion collector (ICS) with 8 μm Al filter and an unshielded ion collector (ICD). On the basis of the TOF method the energy of Au element and the H impurity was calculated. The shielded collector measured only the noise, the Au and H ions were stopped in the Al foil in accordance with the SRIM simulations.

The second experiments was made with the Cu target at laser frequency 1ω and energy of about 300 J.

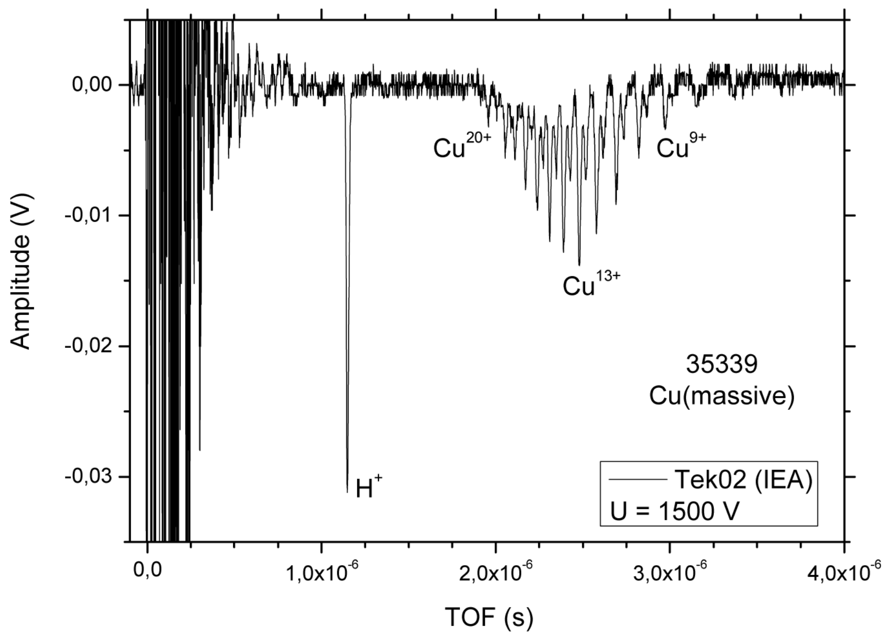

Figure 3.16: Result in TOF configuration using IEA. There are visible peaks from Cu^{9+} up to Cu^{20+} and also hydrogen impurities.

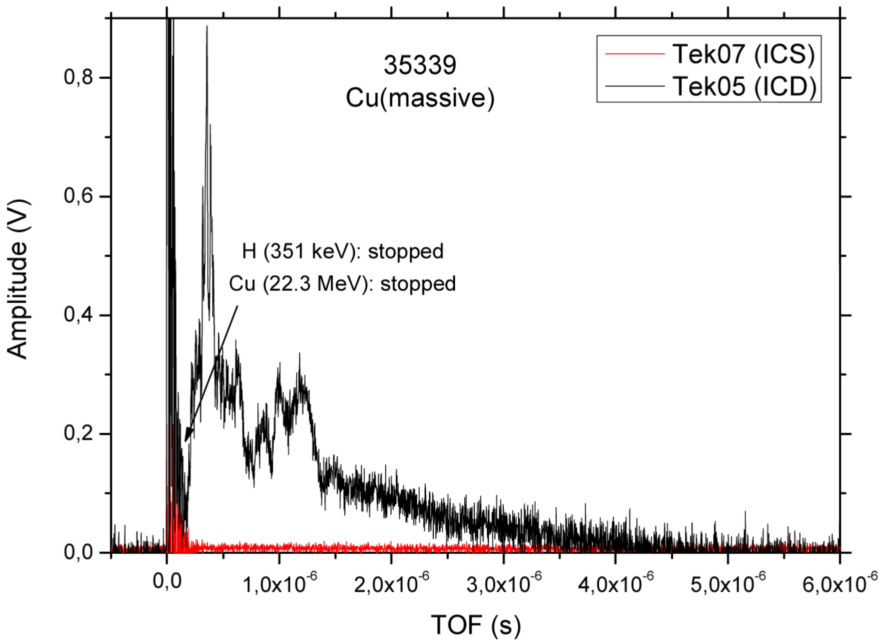

Figure 3.17: Result in TOF configuration using ICS with 8 μm Al filter and ICD. On the basis of the TOF method the energy of Au element and the H impurity was calculated. The shielded collector measured only the noise, the Au and H ions were stopped in the Al foil in accordance with the SRIM simulations.

The third experiment was made with the graphite target at laser frequency 1ω with energy about 500 J. In this measurement the shielded ion collector (ICS) and the ring ion collector (ICR) were used. They were placed at the same angle and at similar distances (ICS was placed several centimetres behind the ICR). The focal spot position varied in the range -200 to 200 μm. Thomson parabola (TP) was also used during these experiments.

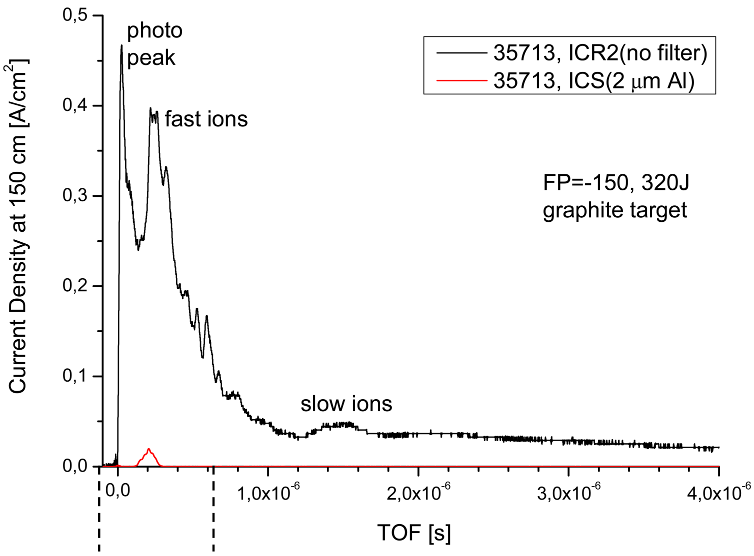

Figure 3.18: Result in TOF measuring using ICS and ICR. The energy of the laser was 320 J and the focal spot was aimed 150 μm inside the target. Part of the plot between the dashed lines is zoomed in the following figure.

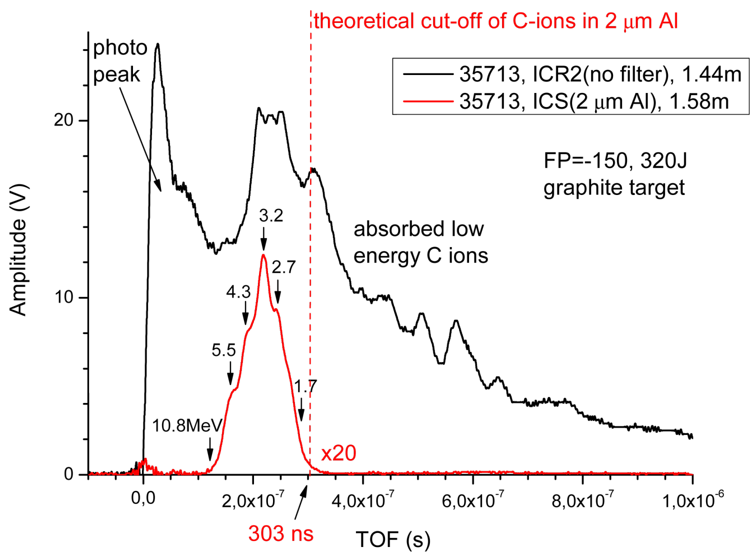

Figure 3.19: Result in TOF measuring using ICS and ICR detectors. The output signal from the ICS is 20 times greater in this figure just to see the clear profile of the shielded collector. It is seen that 2 μm Al foil cut the photopeak and fast ions passed through. The numbers at the partial peaks of the shielded output signal is the energy in MeV of the ions.

The output signal from the shielded detector is composed of ion peaks dedicated with different mass or charge state. The signal presents the convolution of the C^{1+} up to C^{6+} peaks and H^+ also contributes at the beginning of TOF spectrum until it is cut by the Al filter. The number above the red curve in figure 3.19 corresponds to the C^{n+} energy in MeV. Energies for H ions would be twelfth of noted C energies. The ion energy distribution can be estimated from the TP spectrum also obtained in this experiment. Using the ICS with a proper ion fit function the energy spectrum of the single charge states can be reconstructed - this process is called deconvolution - and takes also into account the photopeak contribution [35].

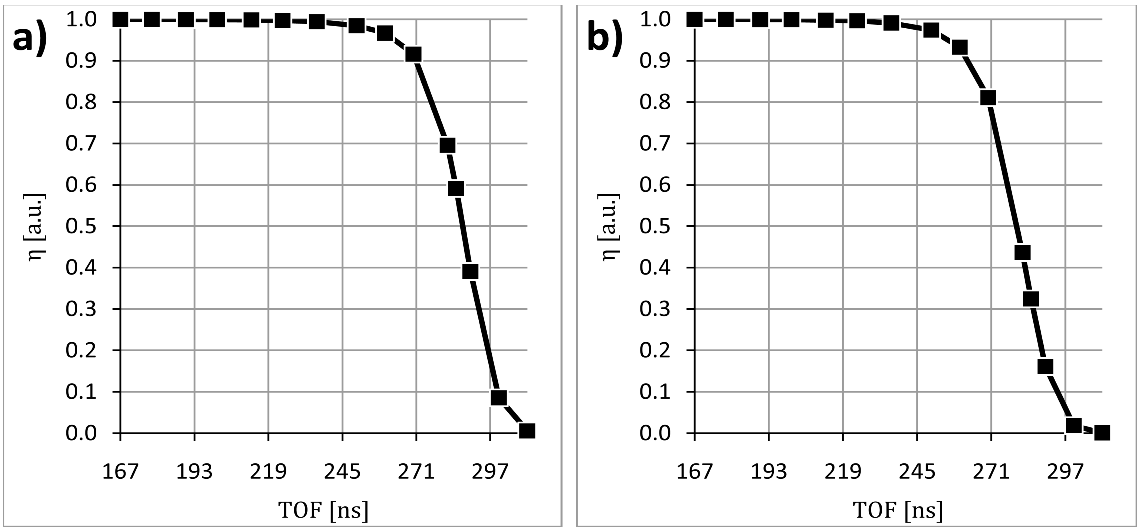

Figure 3.20: Scheme of transparency for C ions calculated by TRIM simulations for measured TOF where a) particle motion is perpendicular to the filter, b) particle motion direction and filter normal make an angle of 15°. The filter is 2 μm of thickness.

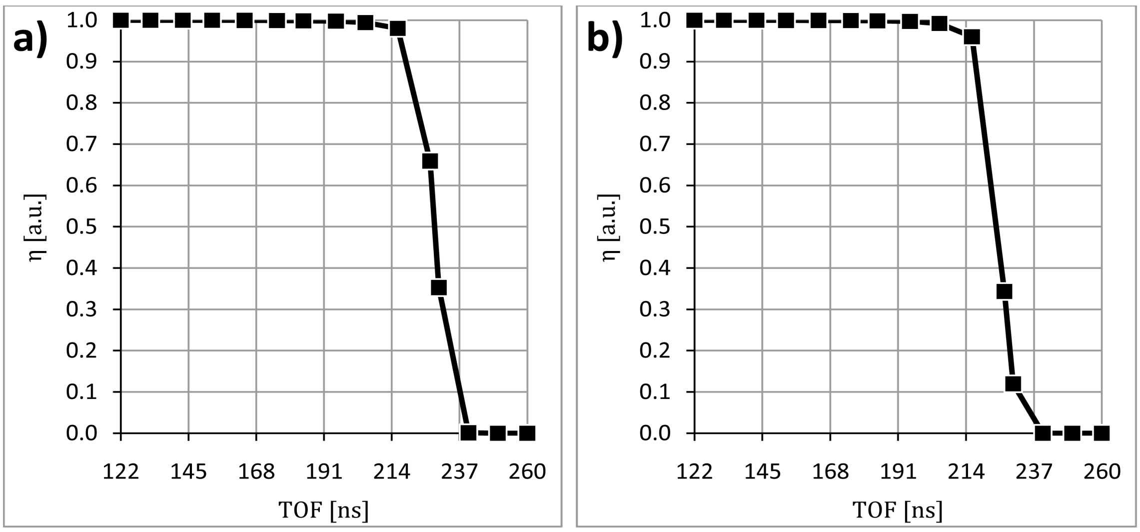

Figure 3.21: Scheme of transparency for H ions calculated by TRIM simulations for measured TOF where a) particle motion is perpendicular to the filter, b) particle motion direction and filter normal make an angle of 15°. The filter is 2 μm of thickness.

Transparency of the filter can be obtained by running the TRIM simulations for certain values of TOF.

In SLPA method, the divergence of accelerated ions is low but it should be mentioned that it is not completely negligible especially when calculating the energy loss in the filter. Entering the filter at an angle means longer propagation through the filter and consequently the greater energy loss. The following two figures show the transparency for carbon and hydrogen entering the filter with different angles with respect to the filter normal.

Chapter 4

Exploration of possible applications

4.1 Accelerator technology

The principal advantages of laser driven electron acceleration over conventional techniques can be clearly identified. Laser driven electron accelerators is extremely compact source, electrons are accelerated in field up to 100–1000 GV/m in comparison with 10–100 MV/m by conventional methods. Acceleration of electrons to the GeV scale may be possible within dimensions of about 1 cm. It is predicted that in the future sub-femtosecond bursts will be generated with the number of electrons reaching over 10^{10} electrons.

The laser driven ion source can be considered as a separate compact ion accelerator. It can be used as an ion injector in large conventional accelerators. The advantage of the laser ion injector is the high ion current, small transverse and longitudinal emittance and the possibility of production of ions at high charge states of arbitrary elements. For successful application of laser driven ion sources in acceleration technology the wider energy spectrum has to be reached. In order to produce ion beams in the GeV energy range, the laser system has to reach intensities greater than 10^{23} W/cm^2 [8].

4.2 Inertial fusion

One of the most important applications of laser driven ion beams is inertial confinement fusion (ICF) in the so-called fast ignition (FI) scheme. Deuterium-tritium (DT) fuel is compressed by high energy lasers with nanosecond pulse durations (X-ray beams can be also used). In conventional ICF the hot spot in the middle of the compressed target has to be formed where the fusion process starts and spreads into the remaining sections of the target.

In FI scheme the compressed DT fuel can be ignited by a separate energy source (as shown on figure 4.1) such as an ultraintense particle beam. The most studied FI scheme counts with a laser driven relativistic electron beam as an ignitor where electrons directly create the ignition hot spot. In the other scheme the multi MeV proton beam is proposed as the ignitor which promises higher beam-fuel coupling efficiency. In this scheme, the electrons accelerate protons that provide the energy for ignition. In both cases the electron beam propagation seems to be the main problem. The electron current is of the order of GA and exceeds the Alfven current limit (maximum current capable to transfer in plasma - if the current is larger than the Alfven current, hot electrons must be influenced by the self-generated magnetic field and the total number of escaping hot electrons is limited, thus the beam current can only propagate while the plasma provides a nearly coincident return current). A cold electron return current must cancel the beam current and it induces a strong ohmic electric field, which can limit the penetration of the beam. The curl of the electric field induces a growing azimuthal magnetic field, up to a limit at which the net current is equal to the Alfven limit. The magnetic field acts to guide or focus the electron beam.

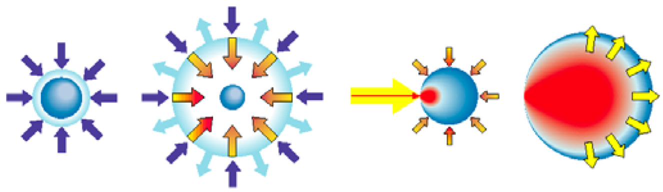

Figure 4.1: Scheme of the DT pellet. Laser beams rapidly heat the surface of the fusion target forming a surrounding plasma envelope. Fuel is compressed by a rocket-like blowoff of the surface material. At the moment of maximum compression a short high intensity pulse ignites the pellet and thermonuclear burn spreads rapidly through the compressed fuel, yielding many times the driver input energy [36].

Using improper laser system leads to strong absorption at its critical density and the problem occurs as the lasers are no longer efficient to reach the implosion. For this case the FI scheme can be improved when a cone is inserted into the pellet in order to provide a path for the ignitor beam.

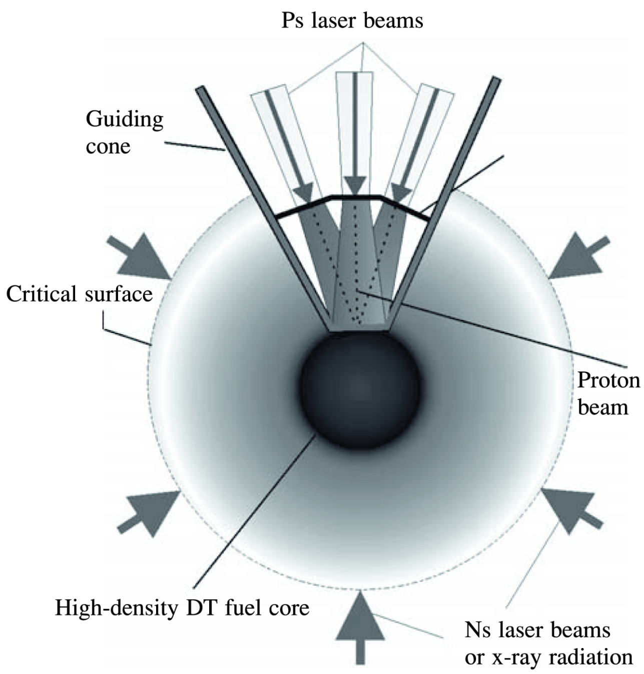

Figure 4.2: Scheme of FI by proton beams produced with the use of SLPA mechanism. High energy ns laser beams compress DT fuel. Picosecond pulses of PW laser beams produce short pulses of high density proton beams which heat a small part of the dense DT fuel core to 10 keV igniting nuclear fusion [8].

There are several requirements for laser driven proton beams to ignite the compressed fuel. Energy of the proton beam has to be in the range 15–20 kJ with proton mean energy 3–5 MeV (proton number will then be approximately 3×10^{16}). The proton beam intensity has to be about 10^{19} W/cm^2 with pulse duration of 10–20 ps and the size of the beam has to be 40 μm (proton density will then be 4×10^{22} cm^{-3}) [37].

4.3 Laboratory astrophysics

The ability of ultrafast ultraintense lasers is to concentrate energy in a small volume capable to create warm-dense matter (WDM) with temperature and density characteristic of star nuclei. Solid density matter can be heated to temperature over 1 keV whereas the pressure inside this matter is far higher than any other pressure found naturally on the Earth and approaches pressures created in nuclear weapons and ICF implosions. Under these conditions the ion-ion potential energy is comparable to the thermal energy. To simulate conditions existing in some astrophysical objects the WDM has to be created by the isochoric heating of matter with a short pulse beam (pulse length of ps or fs) of laser driven ions. Protons can penetrate many microns in a target and this section of the target is heated. This leads to longer disassembly times and fewer gradients. Using PW class lasers as ion beam driver, much more extreme states of matter can be achieved [36].

The highly transient current densities associated with the outflow of the accelerated electrons create azimuthal magnetic fields of the order of hundreds of Tesla approaching those thought to exist on the surface of neutron stars and white dwarfs [36].

Most theories belief that plasmas near a black hole are so hot that matter and anti-matter (electrons and positrons) exist in equilibrium with each other. These matter-antimatter plasmas can be created in laboratory using a PW class lasers. Lasers intensities exceeding 10^{18} W/cm^2 couple most of their energy to superthermal electrons with temperature $kT > mc^2$ where m is the electron rest mass and c is the speed of light. Positrons are created when the relativistic electrons interact with high-Z target ions. High magnetic fields generated by relativistic electrons help to confine them. Particle-in-cell simulations showed positron production for a thin (few μm) gold foil. It also showed that PW class lasers with sufficient pulse length can generate positron densities approximately 10^{22} cm^{-3} for solid gold targets, this result exceeds any laboratory source of positrons [36]. Scheme of such experiment is reported in figure 4.3.

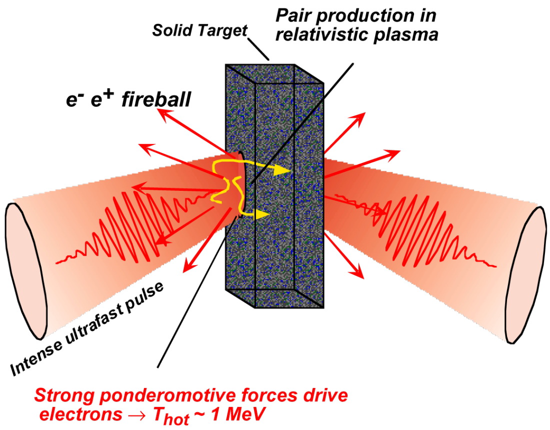

Figure 4.3: Scheme of illumination of a target with two PW laser beams. This experiment could lead to the production of a high density, relativistic electron-positron pair plasma [36].

4.4 Nuclear and particle physics on a tabletop

Short durations and extremely high current densities of laser driven ion beams make possible to do nuclear physics studies in a new time scale with high efficiency of the ion beam - target interaction. Some transient low-cross section nuclear reactions, hardly observable with conventional accelerators, could be feasible to be studied. Using sub-GeV and GeV protons could be efficient for production of pions and muons as well as neutrino beams. Energies of laser produced ions (more than 100 GeV) could potentially open up the opportunity to conduct new fundamental physical research that would range from studies of the strong force to the production of quark-gluon plasmas [8]. More than 100 GeV needs to be available in a particle collision to produce a Higgs boson. All these relativistic energy gains of particles are related to the progress of the laser technologies to reach the laser intensities much higher than 10^{20} W/cm^2.

4.5 Material science and technology

Ion implantation is an example of the use of accelerated ions. It is possible to modify the surface of materials and to improve their properties significantly. The other application of laser driven ion beams is proton radiography. The ultra short proton source is used for high-resolution projection imaging of compressed matter targets, biological objects and also strong transient electric fields in various media. This method uses pulsed monoenergetic quasi-isotropic proton source (pulses about 0.1 ns and energy of 15 MeV FWHM) [38]. Electric and magnetic fields in tested subjects are revealed in radiographs through deflection of the proton trajectories and areal densities are quantified through the proton energy loss while travelling inside the subject.

Energetic electron beams produced by laser plasma accelerators may be used to generate secondary radiation sources of interest for non-destructive material inspection with potential applications in motor engineering and aircraft inspection (γ radiography). The electron beam energy is efficiently converted into multi-MeV bremsstrahlung photons when interacting with a solid target of high atomic number, providing a sub-millimetre pulsed γ-ray source that is significantly smaller and with a shorter duration than other sources. γ-ray sources may be used for monitoring fast moving objects or visualization of high-density metal compression.

An ultra short burst of γ-rays together with the high energy protons can be used to create short-lived radio-isotopes, through [γ,n] and [p,n] reactions. Electron accelerators are potential sources for generating radioisotopes but the beam intensity has to be increased and targets to proper generation of radioisotopes have to be developed. It is an alternative approach to conventional accelerator technologies for short-lived isotope production for various medical and material applications.

4.6 Medicine

The most mentioned medical applications of laser driven ions are the proton cancer therapy and positron emission tomography. Nowadays the cyclotrons or synchrotrons are being used for these purposes. Such devices are large and very expensive. The use of laser-plasma accelerators seems to be the promising way because of their compactness, moderate cost and additional capabilities of controlling of the ion beam parameters.

Proton beams have many advantages in comparison with other kinds of ionizing radiation used for the cancer therapy. Radiotherapy can restrict tumour growth, this works by delivering high doses of X-rays into the body so that enough molecules are ionized to damage tumour cells [39]. Protons in a particle beam should be able to target tumours more precisely than X-rays because protons lose most of their energy just before coming to a standstill when travelling through matter. Thus maximum ionization will occur as the protons approach their stopping point, which depends on the energy of the beam, leaving healthy tissue largely untouched. The basic proton beam parameters required for the cancer therapy are attainable with the use of present laser technology - the beam intensity of 10^{10} protons with a maximum proton energy of 200–250 MeV [8]. The main requirement for proton therapy is that the proton beam must be highly monoenergetic. The energy spread has to be less than 1%. High repetition rate laser systems are necessary for implementation of this technique in the clinic therapy [8].

The parallel development to proton therapy is medical proton tomography. It is an advanced form of medical imaging which has higher resolution and is less invasive to body tissue in comparison with conventional X-ray imaging. Tomography requires proton energies of 100 MeV [36]. Laser-based sources allow the development of this advanced form of medical imaging and will turn it into practical systems. In the positron tomography, positrons from β^+ disintegration of short-lived radioactive isotopes are used. These isotopes are produced by the bombardment of suitable elements with protons, deuterons or alpha particles of energies of several MeV.

4.7 New facilities related to laser-plasma interactions

High Power laser Energy Research (HiPER) is an international project aimed to build an experimental laboratory in which should be proved that thermonuclear fusion is feasible and it can be used as an energy source. Other areas of scientific interest will be studied at HiPER, e.g. the behaviour of matter in extreme conditions (millions of degrees temperature, pressure of billions of atmospheres, magnetic fields a billion times stronger than that of the Earth); WDM which have direct relevance to planetary geophysics and evolution of Earth-like and giant gaseous planets; evolution of highly compressible, nonlinear flows transition to turbulence; laser-plasma interactions under highly nonlinear conditions; production and interaction of macroscopic amounts of relativistic matter; fundamental physics at the strong field limit such as physics of the quantum vacuum.

National Ignition Facility (NIF) is a USA project focusing on ICF and photon science. From mercury laser system 192 laser beams are delivered by a set of deformable mirrors into a spherical configuration of the interaction chamber so that the beams can be focused into the centre of the target chamber. The ICF experiments should demonstrate fusion of the DT capsule and the indirect ignition of the target inside a hohlraum. The laser pulses are delivered onto the inside walls of the hohlraum producing homogenous X-rays and ICF. Photon science at NIF is associated with the research of the advanced optical components and technology, radiographic and energetic system. Other sets of experiment associated with laboratory astrophysics, WDM, high field science etc. will be performed.

The Laser Mégajoule (LMJ) is the French military program devoted to laboratory experiments on the behaviour of materials under very high temperature and pressure conditions. It also has applications in the field of astrophysics, inertial fusion energy (IFE) and fundamental physics. The facility is designed with the maximum flexibility in terms of pulse duration (from 200 ps to 25 ns) and power. Plasma diagnostics will be easily interchanged depending on the type of experiments. The LMJ is designed to deliver 2 MJ radiation in 240 beams (9.5 kJ per one beam at wavelength of 0.35 μm in less than 9 ns pulses [40]) to targets for high energy density physics experiments and to ultimately obtain ignition and propagating burn with DT targets in the laboratory. Experiments at LMJ will be primary focused on the nuclear weapon industry of France.

Extreme Light Infrastructure (ELI) will be European Centre for high-level research on ultra-high intensity laser, laser-matter interactions at the ultra-relativistic regime. The focused exawatt-class laser system is much more powerful than either the LMJ in France and the NIF in the USA and it will produce intensities greater than 10^{23} W/cm^2. The exawatt power will originate from the attosecond-scale (10^{-18} s) pulses. It will open the investigation of new generation of compact accelerators delivering energetic particle and radiation beams in attosecond duration. Relativistic compression offers the potential of intensities exceeding 10^{25} W/cm^2, which would challenge the vacuum critical field as well as provide a new avenue to ultrafast attosecond to zeptosecond (10^{-21} s) studies of laser-matter interaction [41].

Summary and Conclusions

This work gives a basic overview of principles of particle acceleration based on laser-plasma interactions. Electron beams are generated when a relativistic intensity laser beam is focused inside a supersonic gas jet. Electrons are accelerated in potential wakes behind the laser pulse travelling through plasma. Ions streams are produced from interactions of laser pulses with solid targets. According to the thickness of the target there are two methods for producing ion beams in backward (SLPA method) and forward (TNSA method) direction of the laser beam.

The laser system which is being installed at PALS facility has been described along with experimental setup for generation of electron and ion beams. A magnetic electron spectrometer has been described into details in order to measure the electron energy distribution. Ion collector has been described along with the shielded configuration. Several simulations have been performed about the radiation and particle transmission through the shield. Ion energy measurements have been preliminary tested with the iodine laser system at PALS. All these measurements will be applied in upcoming experiments dedicated to laser driven particle acceleration.

Laser-plasma produced fast particles have various applications in the fields of nuclear and particle physics on table top, material science, medicine and also in fast ignition scheme of inertial confinement fusion. Laser particle acceleration on table top has the potential to replace large and expensive conventional accelerators.

The large interest of the scientific community devoted to the preparatory phase of the European projects ELI and HiPER is the proof of the relevance of this new physical field. I focused my work on the preparation of pilot experiments for fast particle beam production at PALS laboratory and in the near future I hope to continue to test the mentioned diagnostics systems and to provide my contribution to the upcoming experimental campaigns.

Bibliography

[1] Chan, F. F. Úvod do fyziky plazmatu. *Academia Praha* (1984)

[2] Kruer, W. L. The Physics of Laser Plasma Interactions. *Paperback* (2001)

[3] Malka, V. *et al.* Staged concept of laser-plasma acceleration toward multi-GeV electron beams. *Phys. Rev. ST Accel. Beams* **9**, 091301 (2006)

[4] `http://www.rp-photonics.com/encyclopedia.html`
(Accessed June 15, 2009)

[5] Mangles, S. P. D. *et al.* Monoenergetic beams of relativistic electrons from intense laser-plasma interactions. *Nature* **431**, 535–538 (2004)

[6] Katsouleas, T. Electrons hang ten on laser wake. *Nature* **431**, 515–516 (2004)

[7] Malka, V. *et al.* Principle and applications of electron beams produced with laser plasma accelerators. *Journal of Physics* **112**, 1–4 (2008)

[8] Badziak, J. Laser-driven generation of fast particles. *Opto-Electron. Rev.* **15**, no. 1, 1–12 (2007)

[9] Tajima, T. & Dawson, J. M. Laser elektron accelerator. *Phys. Rev. Lett.* **43**, 267–270 (1979)

[10] Aminaroff, F. *et al.* Observation of Laser Wakefield Acceleration of Electrons. *Phys. Rev. Lett.* **81**, 995–998 (1998)

[11] Everett, M. J. *et al.* *Nature* **368**, 527 (1994)

[12] Modena *et al.* *Nature* **377**, 606 (1995)

[13] Gahn, C. *et al.* Multi-MeV Electron Beam Generation by Direct Laser Acceleration in High-Density Plasma Channels. *Phys. Rev. Lett.* **83**, 4772–4775 (1999)

[14] Faure, J. *et al.* A laser-plasma accelerator producing monoenergetic electron beams. *Nature* **431**, 541–544 (2004)

[15] Leemans, W. P. *et al.* GeV electron beams from a centimetre-scale accelerator. *Nature Physics* **2**, 696–699 (2006)

[16] Hafz, N. A. M. *et al.* Stable generation of GeV-class electron beams from self-guided laser-plasma channels. *Nature Photonics* **2**, 571–577 (2008)

[17] Hegelich, B. M. *et al.* Laser acceleration of quasi-monoenergetic MeV ion beams. *Nature* **439**, 441–444 (2006)

[18] Schwoerer, H. *et al.* Laser-plasma acceleration of quasi-monoenergetic protons from microstructured targets. *Nature* **439**, 445–448 (2006)

[19] Faure, J. *et al.* GeV controlled injection and acceleration of electrons in plasma wakefields by colliding laser pulses. *Nature* **444**, 737–739 (2006)

[20] Preliminary Proposal: 15 TW Laser system. *Coherent, Inc.* (2006)

[21] `http://www-conf.slac.stanford.edu/orion/PAPERS/C02.PPT`
(Accessed June 15, 2009)

[22] `http://www.bergoz.com/products/ICT/ICT.html`
(Accessed June 15, 2009)

[23] `http://www.carestreamhealth.com/lanex-screens.html`
(Accessed June 15, 2009)

[24] Limpouch, J. *et al.* Enhanced laser ion acceleration from mass-limited targets. *Laser and Particle Beams* **26**, 225–234 (2008)

[25] Woryna, E. *et al.* Laser and Particle Beams: Pulse Power and High Energy Densities. *Cambridge University press*, 295–306 (1996)

[26] Margarone, D. *et al.* Silver plasma by pulsed laser ablation. *Plasma Sources Sci. Technol.* **17**, 035019 (2008)

[27] Nurullina, R. A. *et al.* Development of Compact Magnetic Analyzers for Magnetic Electron Spectrometers. *Bulletin of the Russian Academy of Sciences: Physics* **72**, 483–486 (2008)

[28] `http://www.vectorfields.com/`
(Accessed June 15, 2009)

[29] Wilks, S. C. *et al. Phys. Rev. Lett.* **69**, 1383–1386 (1992)

[30] Mora, P. *Phys. Rev. Lett.* **90**, 185002 (2003)

[31] Fuchs, J. *et al.* Laser-driven proton scaling laws and new paths towards energy increase. *Nature Phys.* **2**, 48–54 (2006)

[32] Margarone, D. *Rad. Eff. and Def. Sol.* **163**, 463 (2008)

[33] `http://henke.lbl.gov/optical_constants/filter2.html`
(Accessed June 15, 2009)

[34] `http://www.srim.org/`
(Accessed June 15, 2009)

[35] Margarone, D., Krasa, J., Rus, B., Laska, L., Velyhan, A., Mocek, T., Krousky, E., Pfeifer, M., Torrisi, L., Andó, L., Gammino, S., Prokupek, J., Ullshmied, J. *Rad. Eff. and Def. Sol.* (in press)

[36] The Science and Applications of Ultrafast, Ultraintense Lasers. *A report on the SAUUL workshop held* (2002)

[37] Badziak, J. *et al.* Studies on proton beam generation for fast ignition-related applications.

http://www.clf.rl.ac.uk/news/Meetings/10th_fastignition2008/documents/thursday/badziak01.ppt

(Accessed June 15, 2009)

[38] Rygg, J. R. *et al.* Proton Radiography of Inertial Fusion Implosions. *Science* **319**, 1223–1225 (2008)

[39] Navaroz Patel. The Plasma Revolution. *Nature* **449**, 133–135 (2007)

[40] Fleurot, N. *et al.* The Laser Mégajoule (LMJ) Project dedicated to inertial confinement fusion: Development and construction status. *Fusion Engineering and Design* **74**, 147–154 (2005)

[41] http://www.extreme-light-infrastructure.eu/

(Accessed June 15, 2009)

[42] Faure, J. Accélération de faisceaux d'électrons par interaction laser-plasma. *Images de la Physique*, 23–28 (2007)

[43] Glinec, Y. *et al.* Absolute calibration for a broad range single shot electron spectrometer. *Review of scientific instruments* **77**, 103301 (2006)

[44] http://www.hiper-laser.org/

(Accessed June 15, 2009)

[45] https://lasers.llnl.gov/

(Accessed June 15, 2009)

[46] http://www-lmj.cea.fr/html/cea.htm

(Accessed June 15, 2009)